

THE EFFECT OF MODELS OF THE INTERSTELLAR MEDIA ON THE CENTRAL MASS DISTRIBUTION OF GALAXIES

C. R. CHRISTENSEN

Department of Astronomy, University of Arizona, 933 North Cherry Avenue, Rm. N204, Tucson, AZ 85721-0065, USA

F. GOVERNATO AND T. QUINN

Department of Astronomy, University of Washington, Box 351580, Seattle, WA 98195, USA

A. M. BROOKS

Department of Astronomy, University of Wisconsin-Madison, 475 N. Charter St., Madison, WI 53706, USA

D. B. FISHER

Department of Astronomy, University of Maryland, CSS Bldg., Rm. 1204, Stadium Dr., College Park, MD 20742-242, USA

S. SHEN

Institute of Particle Physics, University of California, Santa Cruz, CA 95064, USA

J. MCCLEARY

Department of Physics, Brown University, Box Box 1843, 182 Hope St., Barus & Holley, Providence, RI 02912, USA

J. WADSLEY

Department of Physics and Astronomy, McMaster University, Hamilton, ON, Canada

Submitted to MNRAS

ABSTRACT

We compare the central mass distribution of galaxies simulated with three different models of the interstellar medium (ISM) with increasing complexity: primordial (H+He) cooling down to 10⁴K, additional cooling via metal lines and to lower temperatures, and molecular hydrogen (H₂) with shielding of atomic and molecular hydrogen in addition to metal line cooling. The latter model includes a non-equilibrium calculation of the H₂ abundance, self-shielding of H₂, dust shielding of both HI and H₂, and H₂-based star formation efficiency. In order to analyze the effect of these models, we follow the evolution of four field galaxies with V_{peak} < 120 km/s to a redshift of zero using high-resolution Smoothed Particle Hydrodynamic simulations in a fully cosmological Λ CDM context. Artificial observations were created for the galaxies and compared with real observations. The spiral galaxies produced in simulations with either primordial cooling or H₂ physics have bulge magnitudes and scale lengths very similar to observed galaxies and realistic, rising rotation curves. In contrast, the metal line cooling simulation produced galaxies with more massive and concentrated bulges and with the peaked rotation curves typical of most previous Λ CDM simulations of spiral galaxies. The less-massive bulges and non-peaked rotation curves in the galaxies simulated with primordial cooling or H₂ are linked to changes in the angular momentum distribution of the baryons. These galaxies had smaller amounts of low-angular momentum baryons because of increased gas loss from stellar feedback. When there is only primordial cooling, the star forming gas is hotter and the feedback-heated gas cools more slowly than when metal line cooling is included and so requires less energy to be expelled. When H₂ is included, the accompanying shielding produces large amounts of clumpy, cold gas where H₂ forms. Consequentially, star formation takes place in denser and clumpier gas. Star formation in clumpy gas results in more concentrated supernova feedback and greater efficiency of mass loss. The higher feedback efficiency causes a decrease of low-angular momentum material and formation of realistic bulges. The inclusion of the H₂ model and the resulting increase in feedback enabled the creation of simulations with both realistic metal line cooling of the halo gas and realistic structure within the central kiloparsec.

Subject headings:

1. INTRODUCTION

The central question in Λ -Cold Dark Matter (Λ CDM) galaxy formation is how the gas collected into dark mat-

ter (DM) halos was transformed into the stellar populations we observe in galaxies today. To answer this question, we must understand how the interplay between

the physical processes connected with star formation resulted in the observed stellar content of modern galaxies. These processes include the rate at which gas cools, how it is transformed into stars, and the regulation of star formation by such things as stellar feedback. Historically, it has been very difficult for Λ CDM simulations to reproduce observed stellar bulges and the central regions of rotation curves. In this work, we concentrate on how different models of the interstellar media (ISM) and star formation impact the amount of mass in the central region of the disk galaxies, an area particularly sensitive to changes in the angular momentum distribution (AMD). We demonstrate how substantial redistribution of the angular momentum in simulated disk galaxies can be induced by changes to the ISM and, consequentially, to the star formation and supernova (SN) feedback.

Simulations offer the ideal format for studying the evolution of the non-linear processes that dominate galaxy formation over cosmic time, such as the formation of galactic disks. Disks are created by preserving angular momentum from cosmic torques during the infall of gas (White 1984; Barnes & Efstathiou 1987; Quinn & Binney 1992; Maller et al. 2002; Vitvitska et al. 2002). If the gas infall is smooth, high-angular momentum gas will form a similarly high-angular momentum disk (e.g. Mo et al. 1998; Dalcanton et al. 1997). In order to preserve the disk, large amounts of high-angular momentum material must be maintained throughout the galaxy's evolution.

Artificial angular momentum loss has been shown through galaxy simulations to result from insufficient feedback; gas cools and forms stars too quickly and angular momentum is subsequently lost during mergers (White & Rees 1978; Dekel & Silk 1986; Navarro & Benz 1991; Efstathiou 1992; Katz et al. 1994; Navarro & White 1994; Thoul & Weinberg 1996; Quinn et al. 1996; Navarro & Steinmetz 1997; Sommer-Larsen et al. 1999; Gnedin 2000; Maller & Dekel 2002; Sommer-Larsen et al. 2003; van den Bosch et al. 2003; Robertson et al. 2004; Okamoto et al. 2005; D'Onghia et al. 2006; Hoeft et al. 2006; Governato et al. 2008; Okamoto et al. 2008; Scannapieco et al. 2008; Zavala et al. 2008; Ceverino & Klypin 2009; Dutton & van den Bosch 2009; Kereš et al. 2009; Sales et al. 2010). Further work has shown that angular momentum loss is caused by low resolution through such means as two-body heating and artificial viscosity (Thacker et al. 2000; Sommer-Larsen et al. 1999; Mayer et al. 2001; Governato et al. 2004; Kaufmann et al. 2007; Governato et al. 2007; Naab et al. 2007; Mayer et al. 2008; Piontek & Steinmetz 2011). Other simulations have suggested that disk survival could be aided by reducing star formation efficiency at high redshift (Gnedin & Kravtsov 2010). Recently, simulations have progressed in resolution and the modeling of feedback to the point that angular momentum is conserved and disks of the appropriate size that lie along the Tully-Fisher relation are produced even with active merger histories (Governato et al. 2004; Robertson et al. 2006; Scannapieco et al. 2008; Hopkins et al. 2009b; Agertz et al. 2010; Brooks et al. 2011; Brook et al. 2011a; Guedes et al. 2011).

Importantly, though, even if the initial angular

momentum imparted by tidal torques can be maintained, the resulting galaxies do not match the morphologies of observed galaxies. Although observed disk sizes can be reproduced (Fall & Efstathiou 1980; Dalcanton et al. 1997; Mo et al. 1998; Brooks et al. 2011), *the resulting bulges predicted in Λ CDM are much too large compared to observed bulges* (Bullock et al. 2001; van den Bosch et al. 2001; van den Bosch 2001; Binney et al. 2001; Maller & Dekel 2002; Maller et al. 2002; van den Bosch et al. 2002; D'Onghia et al. 2006; D'Onghia & Navarro 2007). This disagreement is true across all disk galaxy masses, not only at the bulgeless dwarf galaxy scale at which the problem is most severe (Dutton 2009). The discrepancy in the amount of low-angular momentum material argues that some process must alter the AMD of disk galaxies by preferentially remove the low-angular momentum gas that would naturally builds up the central regions and bulges of galaxies.

The most sensitive area in the disk to the amount of low-angular momentum material is the central 1 kpc. In this work, therefore, we focus on how the problem of overly large bulges in simulations is affected by different gas cooling models. The study of the central regions of galaxies in relation to angular momentum has only recently become attainable because of computational demands. Cosmological simulations are necessary to follow the detailed evolution of the AMD. Such simulations, however, are very computationally expensive as they require force resolutions small enough to resolve the inner \sim 1kpc, i.e. < 200 pc so that the inner 1kpc contains at least five resolution units.

A few such simulations that resolve the internal structure of disks have demonstrated recently that low-angular momentum gas can be preferentially removed from the galaxy (Governato et al. 2010; Brook et al. 2011a, 2012; Macciò et al. 2012). In Governato et al. (2010) and Brook et al. (2011a), these outflows led to bulgeless disk galaxies with realistic rotation curves (Oh et al. 2011). Guedes et al. (2011) outlined the creation of a Milky Way-mass galaxy with a realistic bulge-to-total disk mass ratio, created by centralized gas loss. Brook et al. (2011b) demonstrated that the outflows created in these high resolution simulations naturally drive low-angular momentum gas from the galaxy.

The preferential removal of low-angular momentum material is key to correctly simulating the central mass distributions in galaxies. In order for this removal to take place, it is crucial to realize the 3-D structure of the ISM at the scale of star formation. When star formation in simulations is limited to regions with densities comparable to those of observed molecular clouds, gas is able to collect in clumps with densities ≥ 100 amu/cc. When the massive stars in these clumps produce SN, the feedback is highly concentrated, leading to expanding bubbles of hot gas that puncture the disk and naturally drive galactic outflows. Importantly, the ability to resolve these dense star forming clumps allows the gas to reach comparable densities to the DM in the central regions of galaxies. Due to these comparable densities, sudden gas loss caused by SN feedback can flatten the gravitational potential, leading to an expansion of the DM orbits and a flattening of the DM density profile (i.e., a shift from a more cuspy profile to a more cored profile Pontzen & Governato 2011). Hence, both the creation

of outflows that remove low-angular momentum gas and the creation of DM cores rely strongly on star formation happening in regions of high density gas.

A natural and physically-motivated method for ensuring that star formation and feedback take place in high density environments in the simulations is to connect star formation to the radiation-shielded areas of the ISM where H_2 is abundant (Robertson & Kravtsov 2008). In observed galaxies, star formation is strongly correlated with molecular gas (Rownd & Young 1999; Murgia et al. 2002; Heyer et al. 2004; Gao & Solomon 2004; Kennicutt et al. 2007; Blanc et al. 2009; Warren et al. 2010; Bigiel et al. 2010; Schruba et al. 2011; Bolatto et al. 2011). Basing star formation on the H_2 abundance also introduces additional dependencies, such as on metallicity. Because of this metallicity dependency, connecting star formation to H_2 has been shown to lower the star formation efficiency in simulations of the low-metallicity, high-redshift Universe (Gnedin & Kravtsov 2010, 2011; Kuhlen et al. 2012; Krumholz & Dekel 2012). Reducing high-redshift star formation may lower the amount of angular momentum loss during mergers (Hopkins et al. 2009b). However, reducing early star formation cannot be responsible for reducing the amount of low-angular momentum material below the initial AMD of the gas.

As of yet, most simulations that have incorporated H_2 based star formation have only used inefficient thermal SN feedback, making them unable to drive outflows that redistribute the angular momentum of the disk gas. Christensen et al. (2012), however, demonstrated that using both H_2 -based star formation and efficient SN feedback to simulate a dwarf galaxy changed the distribution of star formation and the temperature and density distribution of the gas. In this paper, the addition of shielding with the H_2 physics was largely responsible for the increased amount of dense, cold gas. Furthermore, an H_2 -based star formation recipe limited star formation to such dense gas. This ability of H_2 to influence the location and environment of star formation suggests it could also affect the redistribution of angular momentum through feedback, making it a promising tool to better match observational trends in galaxies.

The possible effect of the inclusion of shielded H_2 gas on feedback efficiency reflects a more general dependency of star formation and the feedback efficiency on the ISM model. The rates of cooling and heating naturally affect the mass, distribution, and clumpiness of the gas disk in galaxies. The ability of gas to accrete onto the disk of the galaxy regulates the amount of gas in the disk and, consequentially, the amount of gas available for star formation (Choi & Nagamine 2009; Schaye et al. 2010; van de Voort et al. 2011). Additional low-temperature cooling in the disk leads to the formation of more clumps, increasing the amount of outflowing gas and further altering the AMD. On the other hand, greater amounts of cooling can also make it more difficult to expel gas through feedback. Guedes et al. (2011) and Governato et al. (2010) have produced galaxies with realistic disk scale lengths. However, both these galaxies were simulated without full metal line cooling, raising the question of how they would fare with a more realistic cooling model. Scannapieco et al. (2008) and Piontek & Steinmetz (2011) allowed for cooling below

10^4 K from metal lines but produced galaxies with unphysically large bulges. Brook et al. (2011a, 2012), and Macciò et al. (2012) also included metal line cooling in their simulations but were able to produce realistic bulges only through the addition of an extra source of energy from young stars.

Here, we analyze the effect of different ISM models on star formation and the AMD in simulations of galaxies. To do this, we simulated a small set of dwarf and spiral galaxies of different masses to $z = 0$ using three different models of the ISM: primordial H+He cooling down only to 10^4 K, the addition of metal line cooling, and both metal line cooling and cooling from shielded H_2 gas. Covering multiple galaxy masses and different observable quantities is necessary to constrain the multivariate problem of the interaction between the ISM, star formation and feedback. We expect that the different ISM models will have less of an effect on the dwarf galaxies because of their smaller metallicities and lower H_2 content. The inclusion of the additional cooling from metals or shielding will, therefore, have less effect on the amount and distribution of cold gas. As the galaxy mass increases, though, they will become more metal rich with larger amounts of cold, shielded gas. The choice of ISM model will, consequentially, have a greater effect on the structure of the ISM and the resulting efficiency of SN feedback. In order to compare our simulations to observations, we generated and analyzed both optical and IR images as well as HI velocity cubes. We then examined several different metrics, including the rotation curves, and the characteristics of the bulges, the structure of the ISM, and the efficiency of feedback to determine the effect of the ISM models.

The paper is organized as follow: §2 discusses the simulations; §3.1 describes the global observational properties of the sample; §3.2 shows the differences in the mass distribution resulting from the introduction of H_2 related star formation; §3.3 describes differences in the ISM caused by the introduction of H_2 ; and §3.4 compares the feedback efficiency. The results are then discussed in §4 and §5 is the conclusion.

2. METHODS: DESCRIPTION OF THE SIMULATION

The simulations described here are part of a new set of high-resolution simulations aimed at studying the formation of field galaxies. Our sample of halos includes two dwarf galaxies (virial masses of a few $10^{10} M_\odot$) and two spiral galaxies (virial masses of several times $10^{11} M_\odot$). The properties of the simulated galaxies are listed in Table 1.

The simulations were computed in a WMAP3 cosmology (Spergel et al. 2007): $\Omega_0=0.24$, $\Lambda=0.76$, $h=0.73$, $\sigma_8=0.77$. Our halo sample was selected from lower resolution cosmological volumes and then re-simulated at much higher resolution using the ‘zoom-in’ technique (Katz 1992). Adopting the zoom-in approach enabled us to have a significant number of high-resolution particles while still following the surrounding large-scale structure. There were more than one million DM particles within the virial radius of each galaxy at $z=0$. For the dwarf (spiral) galaxies the DM, gas, and star particle masses (at the time of formation) were respectively: 1.6 (13) $\times 10^4$, 3.3 (27.0) $\times 10^3$, and 1.0 (8.0) $\times 10^3 M_\odot$. The force spline softening was 87 pc (170 pc) for the dwarf (spiral) galax-

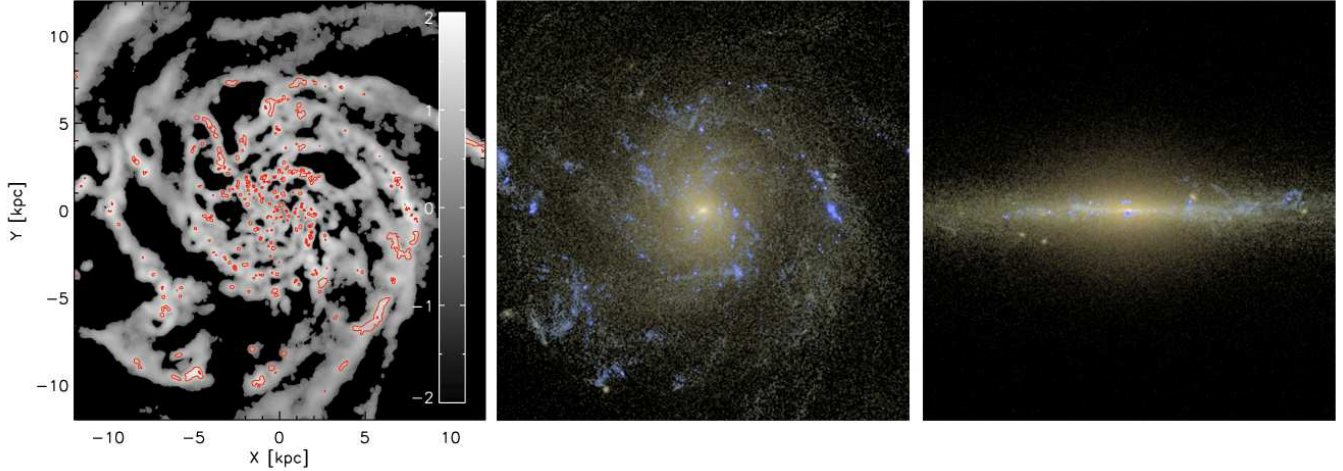


FIG. 1.— Gas surface density and simulated observations of a spiral galaxy (h986) simulated with metal line cooling and H₂ physics. Each frame is 24 kpc across. Left: HI surface density (gray scale) overlaid with red contours indicating the H₂ surface density. The red contours are shown for the following levels: $\log \Sigma_{\text{H}_2} = -2, 0, \text{ and } 2 \text{ amu/cc}$. Middle and right: SDSS multicolor (*r*, *g*, and *i*) images of the same galaxy at $z=0$ generated with SUNRISE in which the galaxy is oriented face on and edge on, respectively. This galaxy has a reddened H-band bulge half light radius, r_e , of 0.83 kpc and a photometric bulge-to-total ratio of $B/T = 0.43$.

ies. The minimum smoothing length for gas particles was 0.1 times the force softening. This resolution was sufficient to follow the formation of star forming regions as small as $10^4 M_\odot$. We further discuss resolution in relation to star formation in §2.2.

The simulations were performed with the *N*-body SPH code GASOLINE (Wadsley et al. 2004) with a force accuracy criterion of $\theta = 0.725$, a time step accuracy of $\eta = 0.195$ and a Courant condition of $\eta_C = 0.4$. The simulations included a cosmic UV field modeled following an updated Haardt & Madau (1996), which partially suppresses the collapse of baryons into the smallest halos (Hoeft et al. 2006; Governato et al. 2007). Our adopted star formation and SN schemes have been described in detail in Stinson et al. (2006) and Governato et al. (2007). Briefly, the “blastwave” feedback scheme is implemented by releasing thermal energy from SN into gas surrounding young star particles. The heated gas particles have their cooling shut off for a time equal to the momentum-conserving phase of the SN blastwave. This time is typically a few million years and is a function of the local density and temperature of the gas and the amount of energy injected and the cooling.

As described in the following subsection, star formation was limited to cold gas in dense regions, with criteria depending on the ISM model (see §2.2). Only two main free parameters in the SN feedback scheme (the star formation efficiency and the fraction of SN energy coupled to the ISM) were fixed to reproduce the properties of present day galaxies over a range of masses (Governato et al. 2007). Without further adjustments, this scheme has been shown to reproduce the relation between metallicity and stellar mass (Brooks et al. 2007; Maiolino et al. 2008) and the abundance of Damped Lyman α (DLA) systems at $z=3$ (Pontzen et al. 2008).

2.1. Models of the ISM

We computed the simulations using three different ISM models of increasing complexity and their corresponding star formation recipes. In these models, the different heating and cooling rates and the presence or lack

of shielding resulted in varying temperature and density distributions. Because of the different structures of the ISM, interaction between the ISM, star formation, and feedback was also altered. Here we outline each of the models.

All the considered models of the ISM include a calculation of the non-equilibrium ion abundances of H and He. The redshift-dependent UV background radiation was responsible for both gas heating and photoionization. Gas cooling was calculated based on collisional ionization (Abel et al. 1997), radiative recombination (Black 1981; Verner & Ferland 1996), photoionization, bremsstrahlung, and H and He line cooling (Cen 1992).

In our simplest ISM model, the heating and cooling of the gas is due only to the above reactions in the neutral and ionized H and He. For the purposes of this paper, we label this the “primordial” ISM model. Because of the lack of low-temperature coolants in this model, cooling is inefficient below 10^4 K. Gas is, therefore, unable to reach lower temperatures and the formation of high density regions is suppressed by the extra pressure support.

Additional cooling from metal lines (Shen et al. 2010) is included in our second ISM model (labeled “metals” throughout the paper). With the addition of metal line cooling, gas is able to cool more efficiently and to temperatures below 10^4 K. These metal line cooling rates were computed for different gas temperatures, densities, metallicities, and amounts of UV background assuming ionization equilibrium and optically thin gas using CLOUDY (version 07.02; Ferland et al. 1998). The metal line cooling rates were introduced to model the intergalactic medium. In this regime it is safe to assume that the gas is optically thin and that the cosmological UV background dominates the radiation field. In the ISM, however, this assumption can result in an underestimate of cooling rates. In the ISM, the lack of an interstellar radiation field beyond the UV background results in substantially less CII (Christensen et al. 2012), the most important coolant in spiral galaxies. Furthermore, the lack of shielding from photoionizing radiation

prevents the additional formation of cold gas.

Our most sophisticated ISM model (labeled as the “H₂” model) includes the non-equilibrium formation of H₂ (Christensen et al. 2012) in addition to metal line cooling. H₂ forms primarily on dust grains and is dissociated by Lyman-Werner radiation from young stars. It is, therefore, limited to dense regions of the ISM where the gas is shielded from Lyman-Werner radiation. Our model follows the hydrogen chemical network for each gas particle, assuming that the dust fraction is proportional to the metallicity and calculating the incident Lyman-Werner radiation based on the emission from nearby star particles. The model includes self-shielding and shielding by dust to protect H₂ from photo-dissociation; dust shielding is also included when calculating the rates of HI photoionization and photoheating. The inclusion of shielded HI and H₂ strongly decreases the amount of heating from photo-dissociation and ionization and results in the formation of a cold (100 K) ISM. Some additional low-temperature cooling is provided through H₂ collision (Gnedin & Kravtsov 2011). While the more accurate calculation of CII and other low-temperature metal coolants would increase the cooling rates, the formation of cold gas is primarily dependent on the presence of shielding. This model for the ISM is, therefore, an important step toward the accurate modeling of the cold, shielded phase of the ISM where star formation takes place.

2.2. Star Formation

As described in Stinson et al. (2006), star formation in these simulations occurs stochastically in gas that is both sufficiently dense and cool. For a gas particle to be eligible to spawn a star particle in this model, it must have a temperature less than T_{max} and a density greater than ρ_{min} . For eligible gas particles, the probability, p , of a star particle forming is a function of the dynamical time, t_{form} ,

$$p = \frac{m_{gas}}{m_{star}} (1 - e^{-c^* \Delta t / t_{form}}) \quad (1)$$

where m_{gas} is the mass of the gas particle, m_{star} is the initial mass of the potential star particle, and c^* is a star forming efficiency factor.

We used different star formation parameters (c^* , T_{max} , ρ_{min}) based on the ISM model. For both the primordial and metal ISM models, $c^* = 0.1$. We set $T_{max} = 10^4$ K and $\rho_{min} = 10$ (100) amu cm⁻³ for the spiral (dwarf) galaxies in order to select for the gas corresponding to the cold ISM in these simulations. This high density threshold for star formation was intended to limit star formation to gas with densities similar to molecular clouds. The high value for T_{max} reflects the inability of gas in the primordial ISM model or zero metallicity gas in the metal line cooling ISM model to cool below 10⁴ K. Star formation is, therefore, allowed to occur in gas substantially hotter than the ~100K gas of molecular clouds.

When using the H₂ model, we incorporated the abundance of H₂ into the star formation calculation as, star formation is observationally linked to H₂ (e.g. Bigiel et al. 2010). We modeled this connection between star formation and H₂ by making the star formation efficiency a function of the local H₂ abundance:

$c^* = 0.1X_{H_2}$, where X_{H_2} is the fraction of hydrogen in the form of H₂. By making the star formation efficiency a function of the H₂ abundance, we eliminated the need for a high density threshold to restrict star formation to molecular clouds. We, therefore, set the density threshold to the arbitrarily low value of $\rho_{min} = 0.1$ amu. We further limited star formation in this recipe to gas that has undergone molecular cooling by setting $T_{max} = 1000$ K. We tested the sensitivity of star formation to both ρ_{min} and T_{max} when using H₂ and found that changes of a factor of five to either threshold did not significantly alter the star formation. With this star formation recipe, we naturally limit star formation to regions that correspond best to those in observed galaxies. Both the inclusion of H₂ and the H₂-based star formation recipe were tested on a cosmological dwarf galaxy in Christensen et al. (2012) and found to produce a bluer dwarf galaxy at $z = 0$ with more extended star formation and clumpier gas.

The high density thresholds for star formation in combination with the low temperature cooling allow gas particles to become Jeans unstable. While this can occur with metal line cooling, the formation of cold gas when shielding is included mean that it is far more prevalent in the H₂ ISM model. Bate & Burkert (1997) showed that when the Jeans length or mass is unresolved artificial fragmentation can occur. At this point star formation becomes dependent on the specifics of the star formation implementation. Many simulators have addressed this by requiring that Jeans instability never occur, either by not including low temperature cooling or adding a pressure floor. Still others made Jeans instability itself the criteria for star formation. We allow Jeans instability to occur with the understanding that gas particles that are Jeans unstable will soon form stars and that the highly efficient SN feedback will heat the surrounding gas, preventing further collapse. While this method does make the star formation dependent on the implementation, Jeans instability is a natural occurrence and it would be equally artificial to prevent it. We see no evidence of artificial collapse in our simulations. We caution, however, that these simulations should not be used to study phenomena occurring below our resolution limit, such as the mass-spectrum of molecular clouds.

2.3. Mock Observations of the Simulated Galaxies

In order to properly compare the outputs from our simulations to real galaxies, we calculated the *observable* properties of the simulated galaxies. These properties include the photometric images, photometric surface brightness profiles, star formation rate (SFR) indicators, and gas surface densities of the galaxies. The observed properties of the four main halos are listed in Table 1 and the methods for calculating them are described below.

The central galaxies in each simulation were first identified using AHF (Gill et al. 2004; Knollmann & Knebe 2009, AMIGA Halo Finder,). AHF adopts overdensities as a function of redshift from Gross (1997), with an overdensity of ~100 with respect to the critical density, ρ_{crit} , at $z = 0$. The environment density at $z = 0$ is typical of field halos with moderate over-underdensity $\delta\rho/\rho = -0.3\text{--}0.3$ measured over a sphere of radius 3 h⁻¹ Mpc. The virial mass, gas mass, cold gas mass (defined as the atomic and molecular hydrogen mass multiplied

by a factor of 1.4 to account for helium), and stellar mass of the central galaxies (defined as the stellar mass within the virial radius that is not within satellites) are listed in columns 1-4 of Table 1. The galaxies simulated with the H₂ ISM model were previously analyzed in (Munshi et al. 2012), in which they were shown to lie along the observed stellar mass-halo mass relation. The asymptotic circular velocities of the galaxies are listed column 5 of Table 1 and the method used to calculate them is described in §3.1.

A direct comparison with observations is vital to judge the realism of the simulated galaxies. We used the Monte Carlo radiation transfer code, SUNRISE (v 3.6 Jonsson 2006) to generate artificial photometric images (see Figure 1) and spectral energy distributions (SEDs) of the simulated galaxies. The magnitude and photometric images of our galaxies in Sloan Digital Sky Survey (SDSS Adelman-McCarthy et al. 2006) bands, Johnson (1966) bands, and Two Micron All Sky Survey (2MASS Cohen et al. 2003) bands were calculated by using SUNRISE to convolve the generated SED with the filter transmission curves. The SDSS *i*-band magnitude of each galaxy is listed in column 6 of Table 1 and the SDSS *g* - *r* color is listed in column 7 of Table 1.

We used the SUNRISE-generated photometric images to calculate the surface brightness profiles of the spiral galaxies and decompose them into bulge and disk components. In order to measure this bulge-disk decomposition of the simulated spiral galaxies, we executed the same analysis discussed in detail in Fisher & Drory (2008). We opted to use the face-on 2MASS H-band images, as infrared data are less sensitive to the obscuring effects of dust and the face-on orientation provides the most accurate fit. For each simulated galaxy, we determined the surface brightness profile through ellipse fitting. Ellipse fitting was done using the routine of Bender & Moellenhoff (1987) using isophotal ellipses of 256 equally spaced points increasing in radius. The software returns surface brightness, isophotal center (in X & Y coordinates), major and minor axis length, and position angle of the ellipse. The radial size of ellipses were optimized to maintain a roughly constant signal-to-noise across the profile. For every galaxy, we also fit isophotal ellipses to the image with the software of Lauer (1985), which is a Fourier based ellipse fitting method. This fit was used as an independent check on the quality of the isophotal ellipse fitting from the Bender & Moellenhoff (1987) routine. The isophotes from both the Bender & Moellenhoff (1987) and Lauer (1985) routines were averaged together and the result used for the bulge-disk decomposition.

The bulge-disk decompositions were determined by fitting two components, a Sérsic bulge plus outer exponential disk, to the major axis surface brightness profile. The inner radius cut for the fit was chosen to be 200 pc (\approx the softening length for the spiral galaxies), and the outer radius cut was set to the location where the profile broke from a smoothly varying exponential. Bars were dealt with using the same method as in Fisher & Drory (2008, 2010), in which isophotes that are affected by bars were isolated and masked from the fitting. The bulge half-light radius, bulge Sérsic index, and the bulge-to-total light ratio are listed in columns 8-10 of Table 1.

SUNRISE also enabled us to measure spatially-

resolved SFRs of the galaxies from the 24 μ m and FUV emission observational indicators. We converted these indicators into SFRs using the formula listed in Leroy et al. (2008) in order to make an accurate comparison to the resolved Kennicutt-Schmidt relationship generated for a large set of nearby galaxies in Bigiel et al. (2008) (see §3.3). In order to enable direct comparisons with a larger sample of observed galaxies, we used H α emission to determine the SFR over the entire disk of the galaxy (column 11 of Table 1).

Finally, we measured the gas surface densities of the main halos in a way comparable with THINGS (The HI Nearby Galaxies Survey, Walter et al. 2008) observations through the use of simulated HI velocity cubes. We created a velocity cube for each galaxy by rotating it to 45° angle and convolving each gas particle with the smoothing kernel and HI fraction calculated in GASOLINE. In order to mimic typical THINGS resolution and sensitivity, we proceeded as if the galaxies were at a distance of 5 Mpc. We used 1.5" pixels and applied beam smearing with a full width at half max of 10" to the data. We divided the data into 128 velocity channels, which had widths of 2.6 km/s for the two spiral galaxies and widths of 1.3 km/s for the dwarf galaxies. Finally, we made a sensitivity cut and ignored all emission from cells below the 2 σ noise limit for the THINGS observations, in which $\sigma = 0.65$ milli-Jansky/beam. This velocity cube was used to create images of the HI surface density (Figure 1 and Figure 9) and to compare to the resolved Kennicutt-Schmidt relation (§3.3).

3. RESULTS

3.1. Global Properties of the Galaxy Sample at $z=0$

Here we examine how the different models of the ISM and their interaction with the SN feedback can change both the total mass and mass distribution in galaxies.

The interaction between the cold ISM, star formation, and SN feedback can affect the final baryonic content of the galaxies at $z=0$ by changing the amount of gas expelled by feedback or stripped from the galaxy. We analyzed this effect by determining the location of the simulated galaxies on the baryonic Tully-Fisher (BTF) relation. This relation compares the total amount of baryons in the form of either stars or cold gas within a halo to the rotational velocity and is known to be observationally a very tight relationship. We compared the main halos of our simulations to the BTF from McGaugh (2005), following their observational analysis as closely as possible (Figure 2). We defined V_f to be the asymptotic circular velocity of the gas. In order to calculate V_f , we fit either an increasing or decreasing arctangent function to the rotation curve (not including radii smaller than twice the softening length). The circular velocities, in turn, were calculated from the mass enclosed at each radii. In all cases except one primordial ISM dwarf galaxy, the simulated galaxies lie exactly on the observed values. However, as we will demonstrate below, the metal ISM model leads to a larger central mass distribution and higher rotational velocity in spiral galaxies. As the total baryonic mass increased, V_f increased in such a way that the simulations moved *along* the BTF relation. This constancy across parameters suggests that the BTF is not sufficient as a discriminator between the ISM models, and

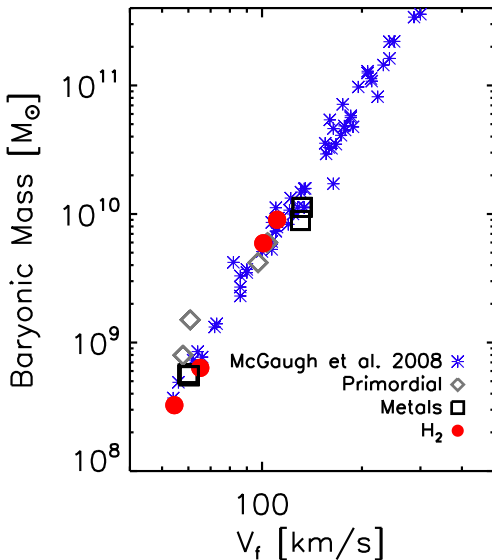


FIG. 2.— Baryonic Tully-Fisher relationship for the main halos overplotted on observational data. Filled red circles represent simulations with H_2 and metal lines cooling (“ H_2 ”); open black squares represent simulations with only metal line cooling (“metals”); open grey diamonds represent simulations with primordial cooling. The blue crosses are observational data from McGaugh (2005). We calculated the baryonic (stellar and cold gas) mass for our simulations in the following way, using the method used in McGaugh (2005) for observed galaxies. The simulation stellar masses were calculated from M_B , using a mass to light ratio determined by the $B - V$ color. The cold gas mass was the total HI and H_2 (when applicable) mass, scaled by a factor of 1.4 to account for helium. As in the observational analysis, we used the asymptotic circular velocity from the rotation curve for V_f . Our simulations, with the exception of one dwarf with the primordial ISM model, lie on the observed data. The tight fit indicates that all ISM models produce galaxies that have the same relationship between central mass and V_f as observed galaxies.

additional diagnostics are necessary.

In addition to comparing the total baryonic masses, we also compared the distributions of matter produced by the different ISM models. Figure 3 shows the circular velocity curves for two of the four main halos (a representative dwarf and spiral galaxy) simulated using the different ISM models. The other two galaxies follow the same trends in mass distribution. These curves show the circular velocity at each radii calculated from the total mass contained within that radii.

We found that all of the ISM models produced continually rising circular velocity curves for the dwarf galaxies. The similarity of the rotation curves for the dwarf galaxies is expected given; the low metallicity and H_2 content of these galaxies would result in relatively small differences between the ISMs produced by the three models. In contrast, the circular velocity curves of the spiral galaxies are very different. Only the primordial and H_2 models produced continually rising rotation curves. The two spiral galaxies simulated with the metal ISM model have a central peak. A comparison sample of observed galaxies is available in de Blok et al. (2008), which provides a set of HI-determined rotation curves for galaxies from THINGS. The gentle rise of the circular velocity

curves for the galaxies simulated with either the primordial or H_2 model is comparable to rotation curves of the observed galaxies. The central peak of the galaxies with the metal model, however, indicates a much higher central concentration and a build-up of low-angular momentum baryons in conflict with observed constraints.

In addition to the rotation curves, the changes to the mass distribution are also apparent in the DM profiles (Figure 4). The DM profiles generated with different ISM models are shown for a representative dwarf and spiral galaxy. The dwarf galaxies experienced only slight changes to their DM profiles and, in contrast to the spiral galaxies, the metal ISM model produced the smallest central concentrations in both h799 and h516. As with the rotation curves, the similarities between the DM profiles can be explained by the low metallicities and molecular content of these galaxies, which reduces the differences between the ISM models. Similarly to the rotation curves, the most dramatic changes to the DM profiles occurred in the spiral galaxies: the DM is most concentrated for the metal simulations and least in the H_2 simulations with the primordial simulations lying in-between. The relatively low concentrations of the H_2 and primordial simulations compared to the metal simulation is consistent with the lack of peaked rotation curves. The changes to the DM profile indicate that the reduced circular velocities seen in Figure 3 are not only the result of reduced central baryonic mass but also to an alteration in the galaxies’s DM distributions.

The changes to the rotation curves and DM profiles denote changes to the AMD. Figure 5 shows the AMD for both the DM and baryonic mass in a representative dwarf and spiral galaxy. The baryons in the plot include all observable baryons, i.e., the stars and the HI and H_2 gas (if applicable) multiplied by a factor of 1.4 to account for the cold helium (helium species are tracked separately from hydrogen in the code). The DM AMD was normalized by dividing by the maximum of the distribution, while the baryon AMD was divided by the maximum and then further scaled by the baryon fraction within the halo (so that a maximum value of 1.0 indicates that the halo has the cosmic baryon fraction). The use of the metal ISM model resulted in a strong peak at zero angular momentum in the spiral galaxy. This peak was caused by a relatively large amount of very low-angular momentum material. In addition to lowering the central peak, both the primordial and H_2 ISM models resulted in less baryonic material in the disks of the spiral galaxies, indicating greater amount of baryonic mass lost from the simulations. As was the case for the rotation curves and DM profiles, the AMDs of the dwarf galaxies show much less variation between models.

3.2. Photometric Decomposition of Galaxies at $z=0$

The reduction of the total stellar mass and the central concentration of baryons in simulations with either the primordial or H_2 ISM raises the question: how do the different models of the ISM affect the distribution of stars in the galaxies? To answer this question, we compared the photometric profiles of the spiral galaxies.

Figure 6 shows the 2MASS H-band radially averaged photometric profiles generated by SUNRISE for a representative spiral galaxy simulated with the different ISM models. From this figure, it is apparent that the pri-

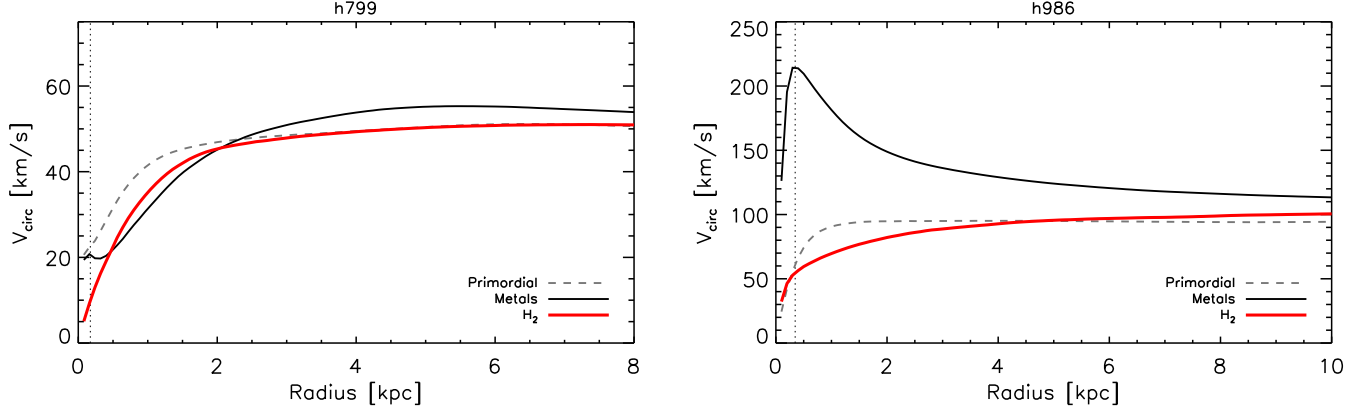


FIG. 3.— The circular velocity profiles of the galaxies. The left panel shows a representative dwarf galaxy (h799) and the right panel shows a representative spiral galaxy (h986). Red lines represent simulations with the H_2 ISM model; black lines represent simulations with the metal ISM model; grey dashed lines represent simulations with the primordial ISM model. The vertical dotted line indicates the radius at twice the softening length. The circular velocity curves of the dwarf galaxies vary only slightly between the different ISM models. Simulations of the spiral galaxies with the H_2 or primordial ISM models have rising circular velocity curves, in contrast to the steeply peaked circular velocity curves of the simulations with the metal ISM model.

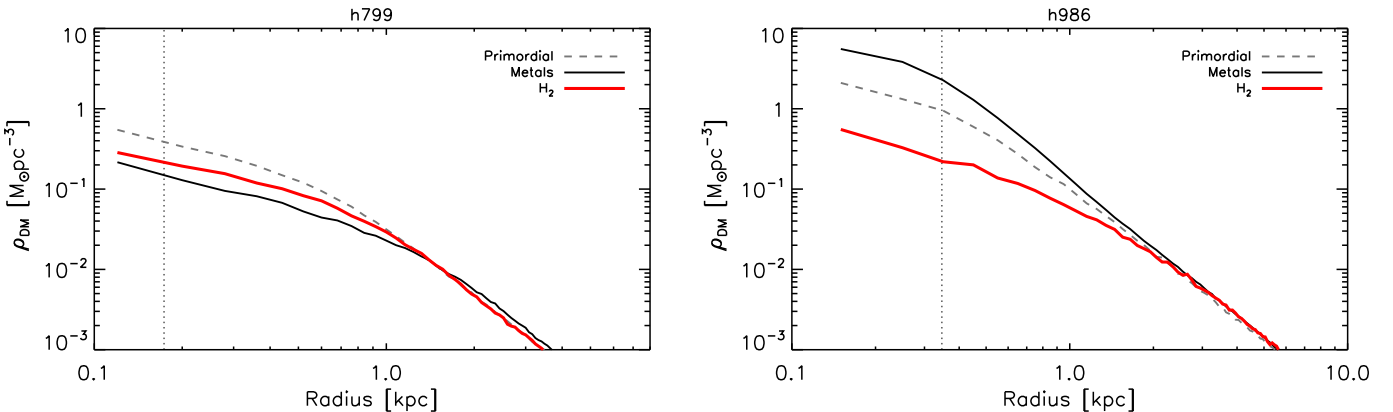


FIG. 4.— Dark matter density profiles of the galaxies. The left panel shows a representative dwarf galaxy (h799) and the right panel shows a representative spiral galaxy (h986). Red lines represent simulations with the H_2 ISM model; black lines represent simulations with the metal ISM model; grey dashed lines represent simulations with the primordial ISM model. The vertical dotted line indicates the radius at twice the softening length. The central densities of the dwarf galaxies are similar across all ISM models. The central concentration of the spiral galaxies is lowest for the H_2 ISM model, followed by the primordial ISM model, and highest for the metal ISM model. This pattern is similar to the changes to the circular velocities with ISM model.

ordial and H_2 models produce galaxies with smaller central surface brightnesses than the metal ISM model. The lower central magnitudes in each denote a less massive bulge and a secondary effect is the expansion of r_e larger.

In order to quantify both the decreased magnitudes of the bulges and larger values of r_e we decomposed the H-band profiles of both the spiral galaxies into an exponential disk and Sérsic bulge using the method outline in §2.3. The values of r_e , the Sérsic index, and the B/T ratio for the two spiral galaxies are listed in Table 1. We compare the bulge H-band magnitudes and r_e for the spiral galaxies with the different ISM models to observed galaxies in Figure 7. The observational data shown is from Fisher et al. (2012 *in prep*). This observed galaxy sample includes spiral galaxies from Hubble types

of Sa to Sd and, therefore, will cover the range of bulge properties. It covers a similar range in B-V as large surveys of galaxies, such as de Vaucouleurs et al. (1991), and preferentially samples bright and large disk galaxies, in which bulges are more commonly found. Galaxies simulated with the primordial and H_2 ISM models have both dimmer and more extended bulges, as seen in the photometric profiles. The reduced magnitude of the bulges occurs in connection to a smaller mass of low-angular momentum baryons in these two simulations. This result is consistent with the observational work of Romanowsky & Fall (2012), which shows different amounts of angular momentum for galaxies of different Hubble types.

The bulges produced with the primordial and H_2 ISM models are more similar to the bulges of observed galax-

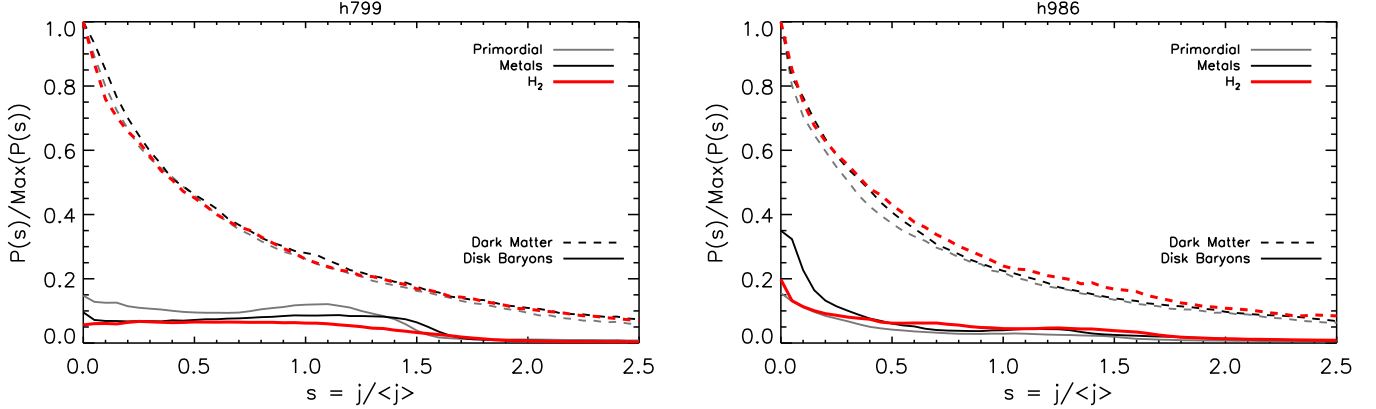


FIG. 5.— The AMD of the DM (dashed lines) and disk baryons (solid lines). Results for a representative dwarf galaxy (h799) appear in the left panel and results for a representative spiral galaxy (h986) appear in the right panel. Red lines represent simulations with the H_2 ISM model; black lines represent simulations with the metal ISM model; grey lines represent simulations with the primordial ISM model. For both the dark matter and baryons, the distribution, $P(s)$, is shown for the angular momentum, j , scaled by the mean angular momentum, $\langle j \rangle$. These distributions of scaled angular momentum are then divided by the maximum of the distribution. For the baryons, the $P(s)$ is again divided by the cosmic baryon fraction to produce the final plot. The baryons used for calculating the angular momentum lie within the optical radii and consist of the stars and cold gas (HI and H_2 gas scaled by a factor of 1.4 for helium). The changes to the AMD are consistent with the changes in the rotation curves. In the spiral galaxies, the use of either the primordial or H_2 ISM model results in decreased baryonic mass in the disk and a smaller mass of low-angular momentum baryons compared to the galaxies simulated with the metal ISM model. In the galaxies with the metal ISM model, the AMD is slightly centrally peaked. The angular momentum profiles of the dwarf galaxies are much more similar, although the galaxy simulated with the primordial ISM model has slightly more disk baryons and the galaxy simulated with the H_2 model has a slightly lower central concentration.

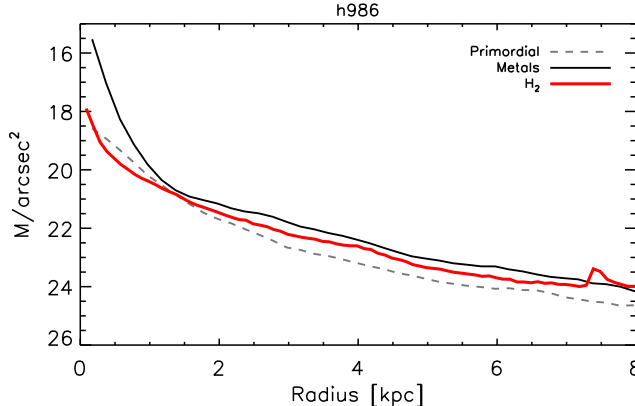


FIG. 6.— Radially binned, face-on photometric profiles in the 2MASS H-band for a representative spiral galaxy (h986). The red line represents the simulation with the H_2 ISM model; the black line represents the simulation with the metal ISM model; the grey dashed line represents the simulation with the primordial ISM model. Simulations with the primordial and H_2 ISM models have reduced central magnitudes.

ies than those produced by the metal ISM model. As can be seen from the observational data, the bulges with the largest r_e are also more luminous (and hence more massive). Rather than move *along* this relation, varying the cooling models in the simulations moves the resulting bulge properties *perpendicular* to this trend. Recall from §3.1 that models moved along the BTF relation, negating the power of the BTF relationship to discriminate between the different models. The perpendicular movement by these models relative to the observed bulge size-luminosity relationship give this relationship greater

discriminating power.

Bulges have older average stellar ages than disks, implying that a large fraction of their stellar mass was formed at comparatively early redshifts (Allen et al. 2006; MacArthur et al. 2009). Furthermore, delayed star formation results in mergers happening between more gas rich galaxies, which leads to the reduced dissipation of angular momentum and smaller bulges (Hopkins et al. 2009a). Given these two effects, we might expect that simulations with smaller bulges would have had less high-redshift star formation. We, therefore, compare the star formation histories for the galaxies with different ISM models to see if they can account for the differences between the bulges.

Figure 8 shows the star formation history for one of the spiral galaxies. We find that both the H_2 and primordial ISM models reduce the total stellar mass of the spiral galaxies, as can also be seen by comparing the data in Table 1. However, the reduction of star formation does not necessarily take place at earlier times. In both galaxies, the star formation in these two models is especially reduced compared to the metal ISM model between 6 and 8 Gyrs. This decrease is likely the result of greater gas-loss from feedback in the primordial or H_2 ISM models. The reduced gas mass in the galaxy limits the amount of star formation in both of these models. The amount of gas loss is further discussed in §3.4.

The use of a H_2 -dependent star formation law has been put forth as a way to reduce early star formation by raising the effective density threshold for star formation in low-metallicity gas (e.g. Robertson & Kravtsov 2008; Gnedin & Kravtsov 2010; Krumholz & Dekel 2012). However, we do not see a significant reduction of the stellar mass prior to 3 Gyrs in the simulations with the H_2 ISM model. After this point in time, the metallicities of the galaxies have increased

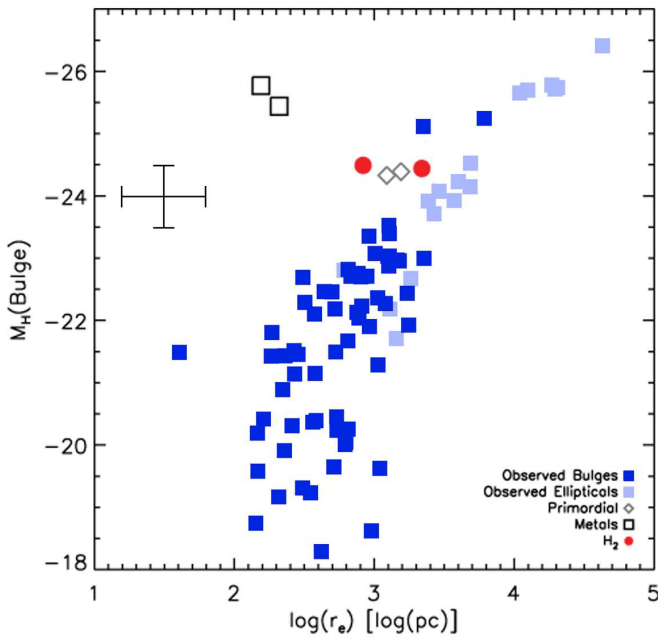


FIG. 7.— Half light radius (r_e) versus magnitude (M_H) of the bulge for the spiral galaxies plotted against observed data. The red filled circles represent simulations with the H_2 ISM model. The black open squares represent simulations with the metal ISM model. The grey open diamonds represent simulations with the primordial ISM model. Observational data is from Fisher et al. 2012 (*in prep*) and marked by dark blue and light blue filled squares, representing observations of bulges and elliptical galaxies, respectively. The black error bars are for the observed data. Both the primordial and H_2 models of the ISM produce dimmer and larger bulges, in closer alignment with the observed galaxies. The metal ISM recipe, in contrast, produces galaxies with an excessive amount of bulge stars.

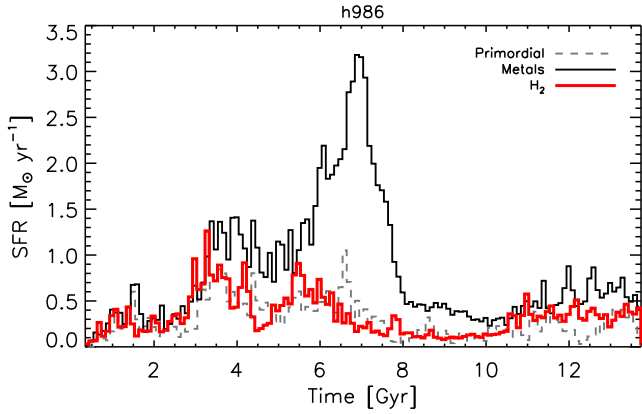


FIG. 8.— Star formation histories of the representative spiral galaxy, h986, produced by each of the models. The red line represents the simulation with the H_2 ISM model; the black line represents the simulation with the metal ISM model; the grey dashed line represents the simulation with the primordial ISM model. There is a strong decrease in the star formation between 6 and 8 Gyrs for the primordial and H_2 ISM models compared to the metal ISM model. The different models do not, however, have a strong impact on the amount of stars formed before 3 Gyrs.

enough to reduce its effect of the star formation law. As discussed in Christensen et al. (2012), star formation in our simulations is strongly regulated by feedback so the reduced star formation efficiency in low metallicity gas has a relatively small effect.

3.3. Properties of the ISM

In this section, we compare the properties of the ISMs produced with each of the models to understand how changes between them are connected to changes to the mass distribution of the galaxies. The gas surface densities for a spiral galaxy simulated with each of the ISM models are shown in Figure 9. In this figure, the logarithmic HI surface densities at the THINGS resolution and sensitivity are shown in grey-scale. For the H_2 model ISM, the logarithmic H_2 surface density is shown in the red contours. This figure shows the variation in the gas distribution produced by the different ISM models. With increased amounts of cooling, the gas distribution becomes both clumpier and more extended.

First, we analyzed the star formation environments in each of the simulations. To do this, we computed the resolved K-S relation for the four galaxies produced with the three different ISM models, and compared them to the THINGS data outlined in Bigiel et al. (2010) (Figure 10). In finding the resolved K-S relation for our sample of galaxies, we closely followed the observational methods. The SFRs were calculated based on the $24\mu\text{m}$ and FUV emission from SUNRISE simulated observations. The HI surface densities were taken from the zeroth moment of the HI velocity cube, which was computed at the same resolution and sensitivity of a standard THINGS observation. The H_2 surface densities were found directly from the simulation output (i.e. we did not calculate it from the CO emission as was done in observed sample). For each of the galaxies, we divided the SFRs and total hydrogen surface densities within the optical radius into $750\text{ pc} \times 750\text{ pc}$ bins. The results are shown in Figure 10. The SFRs and total hydrogen surface densities of the spiral and dwarf galaxies with each of the different ISM models are represented by the colored contours. The grey-scale filled contour map represents the observed data from Bigiel et al. (2010). In general, the simulated data follow the same trend as the observed data. Because of their low-mass, both the dwarf and low-mass spiral galaxies have surface densities lower than $\Sigma_H \sim 10 M_\odot \text{ pc}^{-2}$ and lie on the HI-dominated side of the K-S relation. The metal ISM model may have a slightly steeper slope than either the observed galaxies or the two other simulations. The difference, however, is slight and unlikely to have caused the differences in central stellar mass. We, therefore, conclude that differences in the K-S relation between the simulations are not responsible for changes to the bulge. The similarity between the results for the different ISM models also shows that the K-S relation is not a strong discriminator between our ISM models or star formation recipes in this regime.

We next compared the densities and temperatures of the particles that form stars in the each of the models. Figure 11 shows the phase diagram for the gas particles immediately prior to forming stars. The addition of shielding of both HI and H_2 to the simulation with the H_2 ISM model resulted in a build-up of gas at ≈ 100

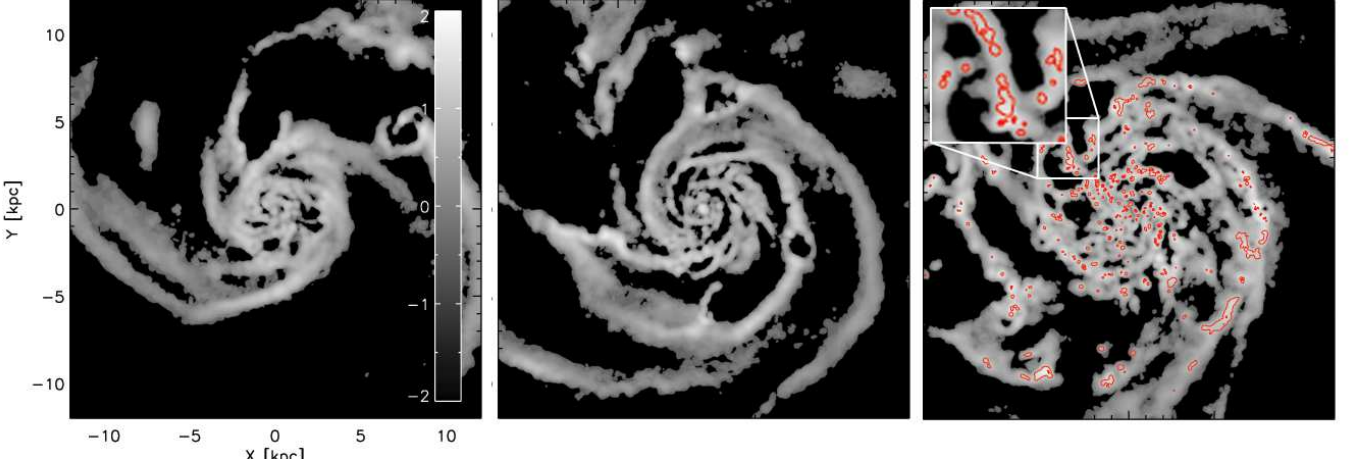


FIG. 9.— Gas surface density of a spiral galaxy (h986) simulated with each of the ISM models: left (primordial), middle (metals), right (H_2). The gray scale is the HI surface density at the THINGS resolution and sensitivity, ranging from $\log \Sigma_{HI} = -2$ to 2 amu/cc. In the right panel, the red contours show the H_2 surface density at $\log \Sigma_{H_2} = -2, 0$, and 2 amu/cc. The clumpiness, amount, and extent of disk gas increase from left to right.

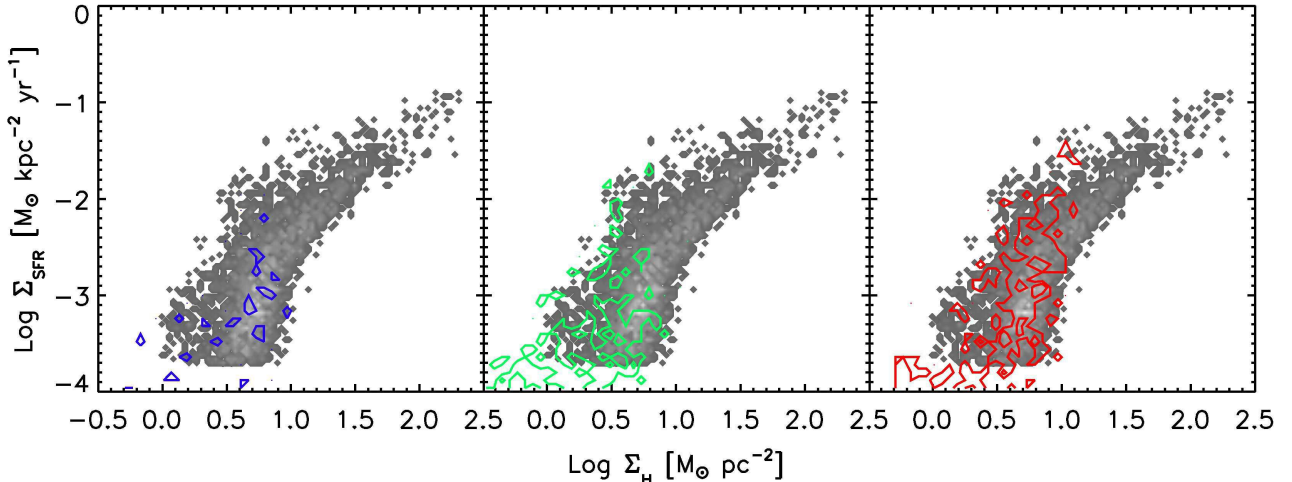


FIG. 10.— Resolved K-S relation for the three different models of the ISM: left (primordial), middle (metals), right (H_2). These plots show the SFRs and total gas (both HI and H_2) surface densities averaged over $750\text{ pc} \times 750\text{ pc}$ bins. The grey-scale filled contours are observational data from Bigiel et al. (2010) for local dwarf and spiral galaxies. The colored contours represent the combined data for the simulated spiral and dwarf galaxies. We calculated the SFRs from the SUNRISE-generated FUV and $24\mu\text{m}$ emission, the HI emission from the face-on velocity cube of average THINGS resolution and sensitivity, and the H_2 directly from the simulation. All the ISM models produced a star formation law on kpc scales that is consistent with the observed data, although the metals ISM model may have a slightly less accurate fit.

K. Furthermore, the H_2 -dependent star formation recipe caused star formation to take place in denser gas with higher H_2 -to-HI fractions. These densities are frequently higher than the current density where gas transitions from HI to H_2 because of the amount of high-redshift star formation that took place in lower metallicity gas and because the delay in star formation after H_2 has formed allows for further collapse. In the metal ISM model, the addition of metal line cooling resulted in star formation taking place at temperatures lower than 10^4K . However, gas in this simulation generally formed stars soon after crossing the 10 amu cm^{-3} density threshold without cooling significantly first. Without additional sources of cooling, gas in the primordial ISM model formed stars at 10^4K . This comparison illustrates how the star forming

gas may be similar when averaged over $\sim 1\text{ kpc}$ scales (as in the resolved K-S law shown in Figure 10) but very different on the smaller scales. These changes to the density of the star forming gas have the potential to affect the efficiency of the blastwave feedback model, with more dense gas resulting in a more concentrated energy.

Changes to the ISM model affect not only the densities of the star forming gas but also the densities of nearby gas particles. The effect of the different ISM models on the gas density and azimuthally-averaged surface density across the disk of the galaxy are shown in Figure 12. In this plot, the three panels represent the different ISM models. Within the optical radii there is little change in the average surface density across simulations. However, the densities of individual particles

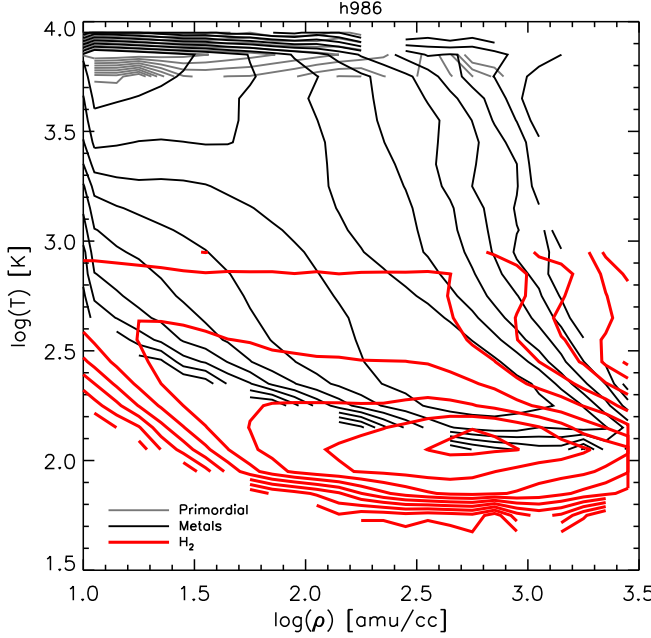


FIG. 11.— Characteristics of the star forming gas in a representative spiral galaxy (h986) simulated with each of the different ISM models and star formation recipes. The contours show the logarithmic distribution of gas particles that formed stars in density and temperature; they represent the number of star particles formed and are spaced linearly. The red contours are for the H₂ ISM model, the black contours are for the metal ISM model, and grey contours are for the primordial ISM model. Compared to the other two models, star formation in the H₂ ISM model takes place in colder gas because of the addition of dust shielding of HI and H₂ and denser gas because of the requirement for gas to be molecular to form stars.

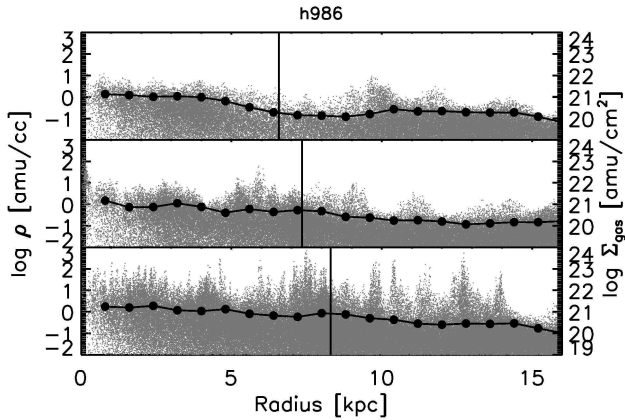


FIG. 12.— Density and azimuthally averaged surface density of gas as a function of radii for a representative spiral galaxy (h986) simulated with the different ISM models. The top panel shows the primordial ISM model, the middle panel shows the metal ISM model, the bottom panel shows the H₂ model. Grey points correspond to the left axis and represent the density of gas particles. The black curves correspond to the right axis and represent the radially-binned average surface densities of the gas. Vertical lines mark the optical radii. The increased cooling from metals and the shielding in the H₂ model resulted in clumpier gas and greater amounts of high density gas although the average surface densities were similar for the different simulations.

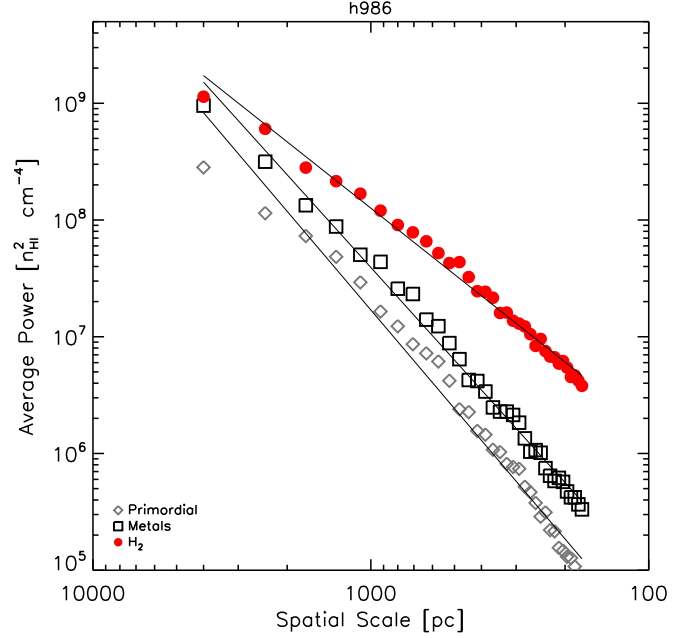


FIG. 13.— Power spectrum of the HI surface density in a representative spiral galaxy (h986). Filled red circles represent simulations with the H₂ ISM model; black empty triangles represent simulations with the metal ISM model; grey empty diamonds represent simulations with the primordial ISM model. The 2-dimensional Fourier transform was calculated on the face-on HI surface density and a power-law was fit to the power spectrum (solid lines). The introduction of H₂ produces a shallower slope than the other two ISM models, indicating that the gas has more power at small scales (i.e. clumpier).

vary substantially between the models. The increased cooling in the metal line model and the shielding in the H₂ model resulted in the gas particles reaching progressively higher densities. High-density star forming regions appear in the plot as spikes in the grey points where gas particles at similar radii have especially high densities. Pontzen & Governato (2011) showed that dense clumps of gas, such as these, are an important factor in the efficiency of SN feedback at transferring angular momentum. When SNe explode, the energy from the blastwave feedback model is concentrated in a smaller number particles than if the star forming gas (and the surrounding gas) was more diffuse. This concentrated burst of energy results in the affected gas particle being heated to higher temperatures and for longer.

The formation of these clumps also allows for star formation throughout a greater extent of the disk. The slight increase in the optical radii (marked by the vertical lines) in the ISM models with more cold gas indicates a greater spatial extent of star formation. As shown in (Christensen et al. 2012), the additional cold gas allows star forming regions to form farther out in the disk of the galaxy in the H₂ simulation.

We quantified the clumpiness of the gas for each of the ISM models using the power spectrum of the HI surface density distribution (Figure 13). We calculated the power spectrum for each of the main halos with the different ISM models by computing a 2-dimensional Fourier transform of the face-on HI surface density using

a Fast Fourier Transform algorithm. For the HI surface density, we used the first moment of the HI velocity cube. However, we did not apply the THINGS beam smoothing or make a sensitivity cut for this analysis as most observations of the power spectra of external galaxies are done with resolutions comparable to or higher than our softening length. We truncated the power spectrum at the force softening length (170 pc in the spiral galaxies). In all simulations, the power spectra can be fit with power laws. The power indicates the relative amount of energy at different scales with shallower slopes indicating greater the energy on small scales, i.e. greater clumpiness. The exponents of the power law fit for h986 (h603) are -2.8 (-3) in the primordial cooling model, -2.6 (-2.7) in the metal cooling model, and -1.9 (-2.1) in the H_2 model. The fits for observed galaxies on scales greater than 200 pc are consistent with these values and have range between -1.5 and -3 (Stanimirović et al. 1999; Elmegreen et al. 2001; Begum et al. 2006; Dutta et al. 2008, 2009). Therefore, we cannot use the power spectrum to distinguish between the accuracy of these models. However, it is clear that the shielding included in the H_2 model produced a clumpier gas with more power at small-scales. We see no strong differences between the power spectra of galaxies with the primordial or metal ISM models. Pilkington et al. (2011), in contrast, detected substantially more power at large scales in a dwarf galaxy run with metal line cooling compared to a dwarf galaxy without it. That galaxy, however, was caught in a state without any on-going star formation, which may account for the enhanced formation of larger-scale structure, such as spiral arms.

3.4. Feedback-Induced Gas Loss

These changes to the ISM have the potential to affect the distribution of gas throughout the galaxy by changing the efficiency of gas loss from feedback. In order to study the efficiency of feedback, we tracked gas particles over the history of the simulation. We followed the history of the most massive progenitor galaxy and traced when gas particles were accreted to it, formed stars, and were ejected. In order to identify the gas particles ejected from the galaxy by SNe, we first identified the gas particles that had been part of the disk of the galaxy ($\rho \geq 0.1$ amu cm $^{-3}$, $T \leq 2 \times 10^4$ K and with a vertical distance to the central plane of the galaxy of less than 10 kpc) at any output. We then looked for subsequent outputs in which the gas particle 1) had been heated by a SN since the time it was first identified as being in the disk and 2) was no longer part of the disk. These two criteria defined the gas particles *ejected* from the disk. We also defined a subset of the ejected gas to be the gas *expelled* from the main halo by selecting particles that traveled beyond the virial radius after being heated by SNe. This gas will only ever again become a part of the galaxy if the virial mass is substantially increased following the expulsion.

This method of identifying outflows is limited by the timestep resolution. The outputs for our simulations are spaced at approximately 350 Myr intervals. Therefore, this method does not identify particles that were ejected from the disk by SNe and then re-accreted onto the disk between two timesteps. Since the simulations all share similar time resolution, however, the results may be used to compare them, even if the accuracy of the absolute

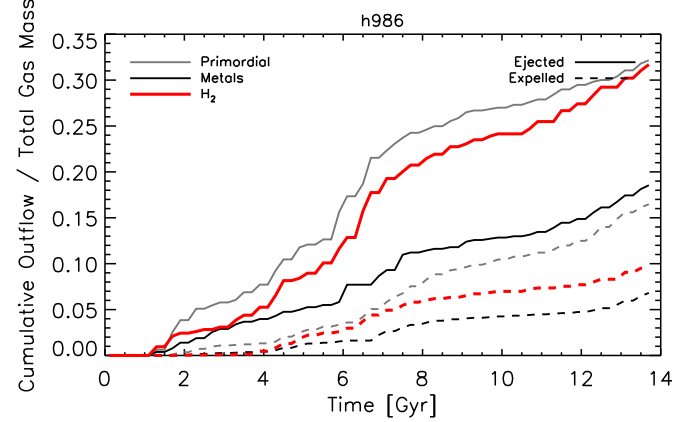


FIG. 14.— Cumulative history of gas loss over the history of the representative spiral galaxy (h986) divided by the amount of gas ever part of the galaxy. Red lines represent simulations with the H_2 ISM model; black lines represent simulations with the metal ISM model; grey lines represent simulations with the primordial ISM model. Solid lines show the fraction of gas ejected from the galaxy disk and dashed lines show the fraction of gas expelled beyond the virial radius. The amount of gas ejected is defined to be the amount of gas what was once in the disk of the galaxy but in some subsequent timestep had been heated by SNe and was no longer within the disk. The expelled gas is the subset of the eject gas that traveled beyond the virial radius of the halo. In order to account for differing amounts of gas accretion, we divided the amount of gas lost by the total mass of gas particles ever contained in the galaxy. The greatest amount of mass loss happens in the primordial ISM galaxy, followed by the H_2 galaxy, and, finally, the galaxy with metal line cooling.

amounts of ejected gas is limited. Within our definition we do not identify the multiple times a gas particle may be ejected from the disk as separate instances but only count the first time.

The mass of gas lost is shown in Figure 14. In this figure, the cumulative histograms of gas ejected from the disk and expelled from the main halo over time are shown for a representative spiral galaxy simulated with the three different ISM models. In order to control for slightly different amounts of gas accretion, the distributions were normalized by the total mass of gas particles ever contained within the virial radius of the main halo. The results for the other spiral galaxy are comparable with the plot shown. The total fraction of gas lost from each of the four galaxies is listed in Table 1.

The effect of the ISM on the spiral galaxies follows the same pattern as the AMD suggests: the the primordial ISM galaxy experienced the most gas loss from feedback, followed by the H_2 galaxy, and finally the galaxy with the metal ISM model. The spiral galaxies simulated with either the primordial or H_2 models also have substantially reduced central concentrations and substantially greater mass loss than the metal ISM model. This pattern supports the theory that feedback is responsible for changing the central mass distribution of galaxies. The difference between the “ejected” and “expelled” gas represents the fraction of gas particles that either remain in the halo indefinitely or are re-accreted onto the galaxy. In the spiral galaxy, h986 (h603), 53 (50)% of the ejected gas in the primordial ISM model is entirely expelled from the galaxy, as opposed to 42 (38)% in the metal ISM model, and 36 (31)% in the H_2 model. The difference in the fraction expelled is caused by the ad-

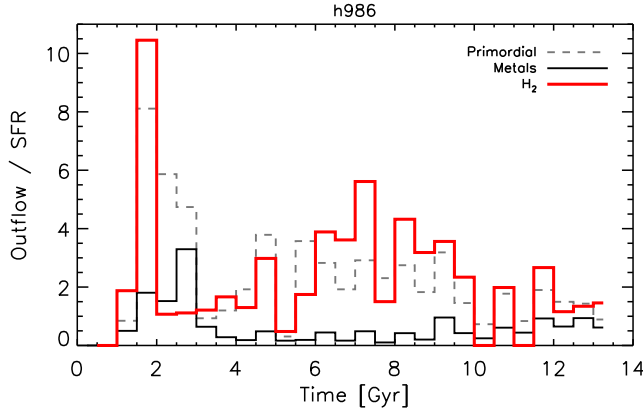


FIG. 15.— Mass loading factor for a representative spiral galaxy (h986) simulated with the three different ISM models. The red line represents simulations with the H_2 ISM model; the black line represents simulations with the metal ISM model; the grey line represents simulations with the primordial ISM model. The mass loading factor is defined in this plot to be the mass of gas ejected from the disk of the galaxy in 0.5 Gyr bins divided by the stellar mass formed during that same time period.

dition of metal line cooling. This addition increases the rates of cooling for ejected gas particles in the halo, making them less likely to be completely expelled. Previous research with simulations has also shown galactic winds can enrich the circumgalactic gas (Oppenheimer & Davé 2006; Ford et al. 2012) and that a substantial amount of gas in galactic winds is re-accreted at a later time (Oppenheimer & Davé 2006; Oppenheimer et al. 2010). Despite our different feedback models and methods for identifying outflows, our simulations appear to be generally consistent with these previous results.

The total amount of gas ejected from the galaxy disk is a function of the SFR. In order to compare the efficiencies of SNe at ejecting gas in these simulations, we divided the mass of gas ejected by the amount of stars formed to arrive at a mass loading factor. The mass loading factor in 500 Myr time bins as a function of time for the representative spiral galaxy with the three different ISM models is shown in Figure 15. In this figure it is clear that both the H_2 and primordial ISM models resulted in greater mass loading than the metal model. This trend is as expected from the comparison of the mass profiles and bulges.

4. DISCUSSION

The correspondence between gas loss and central mass concentration in galaxies illustrates how stellar feedback can reduce the amount of low-angular momentum material in galaxies. The differences between the ISM models are likely the result of two different competing effects. On the one hand, greater cooling results in more cold gas, which requires greater amounts of energy to be expelled from the galaxy. On the other hand, increased gas clumpiness has been shown to lead to more efficient feedback (Governato et al. 2010; Guedes et al. 2011; Governato et al. 2012). When star formation and, therefore, SNe occur in high density peaks in the blast-wave FB model, the energy from SNe is concentrated in a smaller number of gas particles than if the gas and star formation were evenly distributed throughout the disk.

As a result, these particles are ejected farther from the disk and have a larger initial density. Therefore, they have a greater effect on the gravitational potential of the galaxy. The accumulation of these sudden changes to the gravitational potential are what cause the reduction of the central DM concentration over time.

The comparatively high efficiency of gas loss from galaxies with the primordial ISM model was the result of the lower cooling rates compared to the other two models. Gas heated by SNe in this model both starts at higher temperatures ($\geq 10^4$ K) and cools more slowly than when metal line cooling is included. The result of this decreased cooling in our simulations of spiral galaxies was a greater amount of gas ejected farther from the disks. When metal line cooling is added, the temperature of the star forming gas decreases and the cooling rates increases. As a result, greater amounts of energy are required to eject the gas and once ejected, the gas cools and re-accretes onto the disk more quickly. In our simulations, these effects resulted in spiral galaxies with more low-angular momentum material and higher central concentration. A smaller fraction of the gas remained outside of the disk long enough to be identified and being ejected and a smaller fraction was expelled from the galaxy, resulting in smaller mass loading fractions. Other simulations with metal line cooling have anticipated the effect of the increased cooling on feedback and compensated for it by increasing the amount of energy released per SN (e.g. Pilkington et al. 2011). A full comparison such as ours, in which the energy released per SN is held constant, is necessary, however, to find the extent to which the additional cooling affects the matter distribution in simulations.

When H_2 is added, the inclusion of the dust shielding for both HI and H_2 and self-shielding of H_2 results in larger amounts of cold dense gas. In our simulations, the formation of this cold, shielded gas greatly increased the clumpiness of the ISM, as was evident when comparing the gas densities of the particles and the power spectrum of the HI surface density. Furthermore, by linking star formation to the H_2 abundance, star formation was forced to occur in much denser gas than in either the primordial or metal ISM models. Together, the shielding of gas and the H_2 -dependent star formation recipe forced star formation to occur in very dense clumps of gas. While the temperature of the star forming gas was decreased and while the metal line cooling models were still included, the increased clumpiness still produced more efficient mass loss from SN feedback in the spiral galaxies. The concentration of SN energy into the high density, star forming clumps was sufficient in these galaxies to increase the mass loading factor for the ejected gas up to that of the primordial cooling model. Despite the increased amount of ejected gas, a smaller fraction of that ejected gas than in the primordial model was fully expelled from the galaxy because of the metal line cooling of halo gas. This increased feedback efficiency resulted in decreased central concentration and smaller bulges than with the metal ISM model.

These results raise the question: what aspects of the H_2 ISM model primarily caused the differences in the simulations? The first change was the increased amount of cold gas generated by the dust and self-shielding, which resulted in a clumpier ISM. The second change

was forcing of star formation to occur in shielded, dense gas, where the H_2 abundances were high. To first order, both of these effects could be reproduced by implementing a dust shielding model for HI and a star formation recipe that was a function of the local shielding. Star formation laws that are a function of the shielded gas (as opposed to the H_2) has been proposed (Mac Low & Glover 2012; Krumholz 2012; Glover & Clark 2012) as a physical mechanism to explain the observed connection between H_2 and star formation. It is possibly that the time delay introduced by requiring shielded gas to form H_2 may result in subtle differences between H_2 -based and shielding-based star formation laws. In the future, detailed simulations may be able to tease the effects apart.

In contrast to the spiral galaxies, the dwarf galaxies show much less variation in their profiles and gas loss. The smaller dependency of the dwarf galaxies on the ISM model is the result of their lower metallicity. Lower metallicities result both in less metal line cooling and less molecular hydrogen. Therefore, the resulting ISMs are more similar across the different models. The contrast between the dwarf galaxies and spiral galaxies illustrates the importance of testing galaxies of different masses.

Our analysis also demonstrates how two of the more common metrics for analyzing galaxies, the Tully-Fisher relation and the K-S relation, are not sufficient for comparing galaxy models. We found that our galaxies moved along the Tully-Fisher relation as both the mass of the disk and the circular velocity of the disk increased together. The Tully-Fisher relation was, therefore, insensitive to significant changes to the total baryonic mass and central mass distribution. Both the rotation curves and the bulge properties were much more sensitive probes of changes to the AMD and provide stronger observational constraints.

We also found that our very different ISM models and star formation criteria were all able to produce galaxies that all lay along the resolved K-S relation. Even when measured over 750 pc squares, small-scale variations in the ISM were washed out. Furthermore, in these simulations feedback is such a strong regulator of star formation that differences between the star formation thresholds and star formation efficiency had a relatively small effect. We found the gas particle densities and HI surface density power spectrum to provide a more sensitive comparison of the structure of the ISM produced with each of the models.

5. CONCLUSIONS

We analyzed a set of high-resolution dwarf and spiral galaxies computed with three different ISM models: 1) primordial cooling only, 2) metal line cooling and 3) metal line cooling with gas shielding, non-equilibrium H_2 formation, and an H_2 -based star formation recipe. These galaxies were simulated in a cosmological context to a redshift of zero. In order to make our results most comparable to observational data, we analyzed the stellar distribution and mass and the density structure of the ISM at $z = 0$ in an observationally motivated fashion through the creation of simulated optical images and HI velocity cubes. We determined the effect of different ISM models on the efficiency of feedback in redistributing matter throughout the galaxy and we successfully created spiral galaxies with reduced amounts of low-angular momen-

tum material. We found the following results for our suite of simulations:

- Except for one dwarf galaxy simulated with the primordial ISM model, all galaxies lay along the BTF relation. The changes to the ISM simply caused the galaxies to move along the BTF relation, making it poor discriminator between these models.
- The different ISM models resulted in clear changes to the centers of the spiral galaxies. Spiral galaxies simulated with both the primordial and H_2 ISM model had reduced masses within the central 1kpc compared to the metal ISM model, which was apparent in their realistic non-centrally peaked rotation curves, less concentrated DM, and reduced mass of low-angular momentum material.
- From fitting Sérsic and exponential components to H-band images of our spiral galaxy simulations, we found that both the primordial and H_2 models of the ISM produced realistic bulges, whereas the simulations with only metal line cooling produced too massive of bulges.
- The star formation histories of the spiral galaxies with the metal ISM model showed increased star formation around a redshift of 1 compared to the other two models. However, there is little difference between the star formation histories for the spiral galaxies prior to 3 Gyrs. This similarity at high redshift suggests that the smaller bulges produced with the H_2 ISM model were not the result of reduced star formation efficiency in low metallicity gas.
- All simulated galaxies fell along the observed K-S relation (resolved to bins of 750^2 pc^2). However, the individual star forming particles had very different density and temperature distributions for the different models. In particular, in the H_2 ISM model stars formed from colder and denser gas because of the presence of shielding and the use of an H_2 -based star formation law.
- Increasing amounts of cold gas resulted in clumpier ISMs. The effect was particularly strong for the spiral galaxies with H_2 . These galaxies had shallower power structures and increased amounts of high density gas. The ability of gas to collect in high-density clumps at larger radii resulted in more extended star formation.
- The spiral galaxies simulated with the primordial and H_2 ISM models had greater amounts of gas ejected beyond the disk by SNe and larger mass loading factors. This increased efficiency of feedback was likely responsible for the changes to the central kpc of the galaxies. The galaxies with the metal and H_2 ISM models had smaller fractions of their ejected gas escape beyond the virial radius because of increased cooling in the halo from metal lines.
- The dwarf galaxies simulated with different ISM models had relatively similar structures, including rotation curves and stellar profiles, because

of their smaller metallicities. In these galaxies, there was less potential for metal line cooling and shielding/ H_2 , which decreased the effect of the different ISM models.

The fact that both decreased cooling through lack of metal line cooling and increased cold gas from the shielding in our H_2 -model resulted in decreased bulges and increased feedback efficiency implies that multiple processes are at work in determining the mass of bulge stars formed. Compared to galaxies formed with only primordial cooling, the additional cooling in the metal ISM model meant that more feedback energy was required to expel particles. The result was spiral galaxies with more cuspy DM profiles, greater amounts of low-angular momentum gas, centrally-peaked rotation curves, and bigger and more concentrated bulges. With the addition of our H_2 model, the efficiency of feedback once again increased. In this model, star formed within extremely dense clumps, resulting in a greater concentration of SN energy and a greater likelihood of ejecting gas particles from the disk. The increased efficiency of feedback resulted in spiral galaxies with smaller central DM concentrations and decreased amounts of low-angular momentum material, which led to more realistic rising rotation curves and smaller bulges. *This final model is able to pro-*

duce realistic galaxies by including the metal line cooling necessary for modeling the CGM and the re-accretion of gas onto the disk and by including a model for shielded, molecular gas and the star formation that raised the feedback efficiency enough to produce the observed centers of galaxies.

Forming realistic centers of galaxies requires reducing the amount of low-angular momentum material in galaxies. Together, these simulations reinforce the idea that stellar feedback is an effective way to remove low-angular momentum material from galaxies and to shape the central DM distribution. They also demonstrate that stellar feedback models are inexorably linked to ISM models in simulations. In order to create realistic galaxies, models of feedback, ISM and star formation must work together in a realistic manner.

ACKNOWLEDGMENTS

These simulations were run at NASA AMES and Texas Supercomputing Center. CC acknowledges support from NSF grants AST-0908499 and AST-1009452. FG acknowledges support from HST GO-1125, NSF AST-0908499. TQ acknowledges support from NSF grant AST-0908499.

REFERENCES

Abel, T., Anninos, P., Zhang, Y., & Norman, M. L. M. L. 1997, *New Astronomy*, 2, 181

Adelman-McCarthy, J. K., Agueros, M. A., & Others. 2006, *ApJS*, 162, 38

Agertz, O., Teyssier, R., & Moore, B. 2010, *MNRAS*, 410, 1391

Allen, P. D., Driver, S. P., Graham, A. W., et al. 2006, */mnras*, 371, 2

Barnes, J. E., & Efstathiou, G. 1987, *ApJ*, 319, 575

Bate, M. R., & Burkert, A. 1997, *MNRAS*, 288, 1060

Begum, A., Chengalur, J. N., & Bhardwaj, S. 2006, *MNRAS*, 372, L33

Bender, R., & Moellenhoff, C. 1987, *A&A*, 177, 71

Bigiel, F., Leroy, A. K., Walter, F., et al. 2008, *AJ*, 136, 2846

Bigiel, F., Walter, F., Blitz, L., et al. 2010, *AJ*, 140, 1194

Binney, J., Gerhard, O., & Silk, J. 2001, *MNRAS*, 321, 471

Black, J. H. J. H. 1981, *MNRAS*, 197, 553

Blanc, G. A., Heiderman, A., Gebhardt, K., Evans, N. J., & Adams, J. 2009, *ApJ*, 704, 842

Bolatto, A. D., Leroy, A. K., Jameson, K., et al. 2011, *ApJ*, 741, 12

Brook, C. B., Stinson, G. S., Gibson, B. K., et al. 2011a, *ArXiv e-prints*

Brook, C. B., Stinson, G. S., Gibson, B. K., Wadsley, J., & Quinn, T. R. 2012, *ArXiv e-prints*, 9

Brook, C. B., Governato, F., Roškar, R., et al. 2011b, *MNRAS*, 415, 1051

Brooks, A. M., Governato, F., Booth, C. M., et al. 2007, *ApJ*, 655, L17

Brooks, A. M., Solomon, A. R., Governato, F., et al. 2011, *ApJ*, 728, 51

Bullock, J. S., Dekel, A., Kolatt, T. S., et al. 2001, *ApJ*, 555, 240

Cen, R. 1992, *ApJS*, 78, 341

Ceverino, D., & Klypin, A. A. 2009, *ApJ*, 695, 292

Choi, J.-H., & Nagamine, K. 2009, *MNRAS*, 393, 1595

Christensen, C., Quinn, T., Governato, F., et al. 2012, *ArXiv e-prints*

Cohen, M., Wheaton, W. A., & Megeath, S. T. 2003, *AJ*, 126, 1090

Dalcanton, J. J., Spergel, D. N., & Summers, F. J. 1997, *ApJ*, 482, 659

de Blok, W. J. G. J. G., Walter, F., Brinks, E., et al. 2008, *AJ*, 136, 2648

de Vaucouleurs, G., de Vaucouleurs, A., Corwin, H. G., J., et al. 1991, *Third Reference Catalogue of Bright Galaxies*. Volume I: Explanations and references. Volume II: Data for galaxies between 0h and 12h. Volume III: Data for galaxies between 12h and 24h. (New York, NY (USA): Springer)

Dekel, A., & Silk, J. 1986, *ApJ*, 303, 39

D'Onghia, E., Burkert, A., Murante, G., & Khochfar, S. 2006, *ArXiv e-prints*, 372, 1525

D'Onghia, E., & Navarro, J. F. 2007, *MNRAS*, 380, L58

Dutta, P., Begum, A., Bharadwaj, S., & Chengalur, J. N. 2008, *MNRAS*, 384, L34

—. 2009, *MNRAS*, 398, 887

Dutton, A. A. 2009, *MNRAS*, 396, 121

Dutton, A. A., & van den Bosch, F. C. 2009, *MNRAS*, 396, 141

Efstathiou, G. 1992, *MNRAS*, 256, 43P

Elmegreen, B. G., Kim, S., & StaveleySmith, L. 2001, *ApJ*, 548, 749

Fall, S. M., & Efstathiou, G. 1980, *MNRAS*, 193, 189

Ferland, G. J., Korista, K. T., Verner, D. A., et al. 1998, *PASP*, 110, 761

Fisher, D. B., & Drory, N. 2008, *AJ*, 136, 773

—. 2010, *ApJ*, 716, 942

Ford, A. B., Oppenheimer, B. D., Davé, R., et al. 2012, *ArXiv e-prints*, 25

Gao, Y., & Solomon, P. M. 2004, *ApJ*, 606, 271

Gill, S. P. D., Knebe, A., & Gibson, B. K. 2004, *MNRAS*, 351, 399

Glover, S. C. O., & Clark, P. C. 2012, *MNRAS*, 421, 9

Gnedin, N. Y. 2000, *ApJ*, 535, 530

Gnedin, N. Y., & Kravtsov, A. V. 2010, *ApJ*, 714, 287

—. 2011, *ApJ*, 728, 88

Governato, F., Mayer, L., & Brook, C. B. 2008, in *Astronomical Society of the Pacific Conference Series*, Vol. 396, *Astronomical Society of the Pacific Conference Series*, ed. J. G. Funes & E. M. Corsini, 453–+

Governato, F., Willman, B., Mayer, L., et al. 2007, *MNRAS*, 374, 1479

Governato, F., Mayer, L., Wadsley, J., et al. 2004, *ApJ*, 607, 688

Governato, F., Brook, C. B., Mayer, L., et al. 2010, *Nature*, 463, 203

Governato, F., Zolotov, A., Pontzen, A., et al. 2012, *MNRAS*, 422, 1231

Gross, M. A. K. 1997, PhD thesis, University of California, Santa Cruz

Guedes, J., Callegari, S., Madau, P., & Mayer, L. 2011, *ApJ*, 742, 12

Haardt, F., & Madau, P. 1996, *ApJ*, 461, 20

Heyer, M. H., Corbelli, E., Schneider, S. E., & Young, J. S. 2004, *ApJ*, 602, 723

Hoeft, M., Yepes, G., Gottlöber, S., & Springel, V. 2006, *MNRAS*, 371, 401

Hopkins, P. F., Cox, T. J., Younger, J. D., & Hernquist, L. 2009a, *ApJ*, 691, 1168

Hopkins, P. F., Somerville, R. S., Cox, T. J., et al. 2009b, *MNRAS*, 397, 802

Johnson, H. L. 1966, *ARA&A*, 4, 193

Jonsson, P. 2006, *MNRAS*, 372, 2

Katz, N. 1992, *ApJ*, 391, 502

Katz, N., Quinn, T. R., Bertschinger, E., & Gelb, J. M. 1994, *MNRAS*, 270, L71+

Kaufmann, T., Mayer, L., Wadsley, J., Stadel, J., & Moore, B. 2007, *MNRAS*, 375, 53

Kennicutt, R. C. J., Calzetti, D., Walter, F., et al. 2007, *ApJ*, 671, 333

Kennicutt Jr., R. C., & Kennicutt, R. C. J. 1998, *ApJ*, 498, 541

Kereš, D., Katz, N., Davé, R., Fardal, M., & Weinberg, D. H. 2009, *MNRAS*, 396, 2332

Knollmann, S. R., & Knebe, A. 2009, *ApJS*, 182, 608

Krumholz, M. R. 2012, *ApJ*, 759, 9

Krumholz, M. R., & Dekel, A. 2012, *ApJ*, 753, 16

Kuhlen, M., Krumholz, M. R., Madau, P., Smith, B. D., & Wise, J. 2012, *ApJ*, 749, 36

Lauer, T. R. 1985, *ApJS*, 57, 473

Leroy, A. K., Walter, F., Brinks, E., et al. 2008, *AJ*, 136, 2782

Mac Low, M.-M., & Glover, S. C. O. 2012, *ApJ*, 746, 20

MacArthur, L. A., González, J. J., & Courteau, S. 2009, *MNRAS*, 395, 28

Macciò, A. V., Stinson, G. S., Brook, C. B., et al. 2012, *ApJ*, 744, L9

Maiolino, R., Nagao, T., Grazian, A., et al. 2008, *A&A*, 488, 463

Maller, A. H., & Dekel, A. 2002, *MNRAS*, 335, 487

Maller, A. H., Dekel, A., & Somerville, R. S. 2002, *MNRAS*, 329, 423

Mayer, L., Governato, F., Colpi, M., et al. 2001, *ApJ*, 559, 754

Mayer, L., Governato, F., & Kaufmann, T. 2008, *Advanced Science Letters*, 1, 7

McGaugh, S. S. 2005, *ApJ*, 632, 859

Mo, H. J. J., Mao, S., & White, S. D. M. 1998, *MNRAS*, 295, 319

Munshi, F., Governato, F., Brooks, A. M., et al. 2012, *ArXiv e-prints*

Murgia, M., Crapsi, A., Moscadelli, L., & Gregorini, L. 2002, *A&A*, 385, 412

Naab, T., Johansson, P. H., Ostriker, J. P., & Efstathiou, G. 2007, *ApJ*, 658, 710

Navarro, J. F., & Benz, W. 1991, *ApJ*, 380, 320

Navarro, J. F., & Steinmetz, M. 1997, *ApJ*, 478, 13

Navarro, J. F., & White, S. D. M. 1994, *MNRAS*, 267, 401

Oh, S.-H., Brook, C. B., Governato, F., et al. 2011, *AJ*, 142, 24

Okamoto, T., Eke, V. R., Frenk, C. S., & Jenkins, A. 2005, *MNRAS*, 363, 1299

Okamoto, T., Gao, L., & Theuns, T. 2008, *ArXiv e-prints*, 806

Oppenheimer, B. D., & Davé, R. 2006, *MNRAS*, 373, 1265

Oppenheimer, B. D., Davé, R., Kereš, D., et al. 2010, *MNRAS*, 406, 2325

Pilkington, K., Gibson, B. K. K., Calura, F., et al. 2011, *MNRAS*, 417, 2891

Piontek, F., & Steinmetz, M. 2011, *MNRAS*, 410, 2625

Pontzen, A., & Governato, F. 2011, *ArXiv e-prints*, 7

Pontzen, A., Governato, F., Pettini, M., et al. 2008, *MNRAS*, 390, 1349

Quinn, T., & Binney, J. 1992, *MNRAS*, 255, 729

Quinn, T. R., Katz, N., & Efstathiou, G. 1996, *MNRAS*, 278

Robertson, B. E., Bullock, J. S., Cox, T. J., et al. 2006, *ApJ*, 645, 986

Robertson, B. E., & Kravtsov, A. V. 2008, *ApJ*, 680, 1083

Robertson, B. E., Yoshida, N., Springel, V., & Hernquist, L. 2004, *ApJ*, 606, 32

Romanowsky, A. J., & Fall, S. M. 2012, *ArXiv e-prints*, 61

Rownd, B. K., & Young, J. S. 1999, *AJ*, 118, 670

Sales, L. V., Navarro, J. F., Schaye, J., et al. 2010, *MNRAS*, 409, 1541

Scannapieco, C., Tissera, P. B., White, S. D. M., & Springel, V. 2008, *MNRAS*, 389, 1137

Schaye, J., Vecchia, C. D., Booth, C. M., et al. 2010, *MNRAS*, 402, 1536

Schruba, A., Leroy, A. K., Walter, F., et al. 2011, *AJ*, 142, 37

Shen, S., Wadsley, J., & Stinson, G. S. 2010, *MNRAS*, 407, 1581

Sommer-Larsen, J., Gelato, S., & Vedel, H. 1999, *ApJ*, 519, 501

Sommer-Larsen, J., Götz, M., & Portinari, L. 2003, *ApJ*, 596, 47

Spergel, D. N., Bean, R., Doré, O., et al. 2007, *ApJS*, 170, 377

Stanimirović, S., Staveley-Smith, L., Dickey, J. M., et al. 1999, *MNRAS*, 302, 417

Stinson, G. S., Seth, A. C., Katz, N., et al. 2006, *MNRAS*, 373, 1074

Thacker, R. J., Tittley, E. R., Pearce, F. R., Couchman, H. M. P., & Thomas, P. A. 2000, *MNRAS*, 319, 619

Thoul, A. A., & Weinberg, D. H. 1996, *ApJ*, 465, 608

van de Voort, F., Schaye, J., Booth, C. M., Haas, M. R., & Dalla Vecchia, C. 2011, *MNRAS*, 414, 2458

van den Bosch, F. C. 2001, *MNRAS*, 327, 1334

van den Bosch, F. C., Abel, T., Croft, R. A. C., Hernquist, L., & White, S. D. M. 2002, *ApJ*, 576, 21

van den Bosch, F. C., Abel, T., & Hernquist, L. 2003, *MNRAS*, 346, 177

van den Bosch, F. C., Burkert, A., & Swaters, R. A. 2001, *MNRAS*, 326, 1205

Verner, D. A. A., & Ferland, G. J. J. 1996, *ApJS*, 103, 467

Vitvitska, M., Klypin, A. A., Kravtsov, A. V., et al. 2002, *ApJ*, 581, 799

Wadsley, J., Stadel, J., & Quinn, T. R. 2004, *New Astronomy*, 9, 137

Walter, F., Brinks, E., de Blok, W. J. G., et al. 2008, *AJ*, 136, 2563

Warren, B. E., Wilson, C. D., Israel, F. P., et al. 2010, *ApJ*, 714, 571

White, S. D. M. 1984, *ApJ*, 286, 38

White, S. D. M., & Rees, M. J. 1978, *MNRAS*, 183, 341

Zavala, J., Okamoto, T., & Frenk, C. S. 2008, *MNRAS*, 387, 364

TABLE 1
 GALAXY PROPERTIES

		Virial Mass [M_{\odot}] (1)	Gas Mass in R_{vir} [M_{\odot}] (2)	Cold Gas Mass [M_{\odot}] (3)	Stellar Mass [M_{\odot}] (4)	V_f [km/s] (5)	Mag. <i>i</i> band (6)	$g - r$ (7)	$\log(r_e/\text{kpc})$ H band (8)	B/T H band (9)	Sérsic Index H band (10)	SFR _{H_{α}} [M_{\odot}/yr] (11)	% Gas Lost (12)
h516^{abcdefg}	Primordial	3.9×10^{10}	2.6×10^9	1.4×10^9	2.6×10^8	61	-16.2	0.54	-	-	-	0.004	10
	Metals	3.6×10^{10}	1.7×10^9	4.3×10^8	2.1×10^8	60	-16.1	0.52	-	-	-	0.005	10
	H_2	3.8×10^{10}	2.3×10^9	5.5×10^8	2.5×10^8	65	-16.4	0.42	-	-	-	0.011	12
h799^{abfg}	Primordial	2.3×10^{10}	1.3×10^9	7.0×10^8	1.8×10^8	58	-16.2	0.37	-	-	-	0.001	10
	Metals	2.4×10^{10}	1.5×10^9	3.3×10^8	1.3×10^8	60	-15.5	0.55	-	-	-	-	7
	H_2	2.4×10^{10}	1.4×10^9	1.8×10^8	1.4×10^8	54	-15.6	0.45	-	-	-	0.007	15
h603^{abg}	Primordial	3.1×10^{11}	2.8×10^{10}	2.4×10^9	5.5×10^9	104	-19.1	0.52	3.19	0.58	1.9	0.068	15
	Metals	3.0×10^{11}	2.6×10^{10}	2.8×10^9	1.3×10^{10}	132	-20.5	0.58	2.32	0.59	1.6	0.182	8
	H_2	3.4×10^{11}	3.1×10^{10}	4.2×10^9	7.8×10^9	111	-20.3	0.41	2.92	0.43	1.7	0.389	10
h986^{abg}	Primordial	1.7×10^{11}	1.4×10^{10}	1.7×10^9	4.0×10^9	97	-19.6	0.40	3.09	0.59	2.3	0.023	16
	Metals	1.8×10^{11}	1.5×10^{10}	2.1×10^9	1.1×10^{10}	131	-20.3	0.59	2.19	0.68	2.3	0.354	7
	H_2	1.9×10^{11}	1.7×10^{10}	3.5×10^9	4.5×10^9	101	-19.7	0.32	3.34	0.53	2.5	0.498	10

NOTE. — Properties of the main halos at $z = 0$. The virial mass, gas mass within the virial radius (R_{vir}), cold gas mass, and stellar mass are calculated directly from the simulations. The cold gas is defined as being $1.4(M_{\text{HI}} + M_{H_2})$, where M_{HI} is the total mass of atomic hydrogen, M_{H_2} is the total mass of molecular hydrogen, and the factor of 1.4 compensates for the mass of cold He (He species are tracked separately from hydrogen in the code). In the primordial and metal simulations, the H_2 mass is zero and the hydrogen gas that would be molecular remains as HI. V_f was calculated for each galaxy by fitting an arctangent function to the circular velocities. The SDSS *i*, *g*, and *r* band magnitudes were calculated for a disk inclination of 45° from a simulated SUNRISE observation, which includes dust obscuration. SUNRISE was also used to determine the H-band profile. For the two spiral galaxies (h603 and h986), a Sérsic bulge and exponential disk were fit to the H-band profile. The bulge half light radius (r_e), the Sérsic index of the bulge, and the B/T ratio for these fits are listed in columns 8 – 10. The two dwarf galaxies (h516 and h799), in contrast, were best fit with only an exponential disk. The SFR at $z = 0$ for each of the galaxies was calculated from the SUNRISE-generated H_{α} emission, using the same conversion as Kennicutt Jr. & Kennicutt (1998). The “% Gas Lost” refers to the the mass of supernova-heated gas expelled beyond the virial radius divided by the total mass of gas particles ever within the virial radius of the galaxy (see §3.4 for details).

^a Appears with primordial cooling and an additional low temperature cooling model in Governato et al. (2010). The galaxies are labeled as DG1(h516) and DG2 (h799).

^b Appears with the Primordial ISM model in Brooks et al. (2011). In Brooks et al. (2011), both h603 and h986 are at lower resolution.

^c Appears with the Metal ISM model in Oh et al. (2011) as DG1 (DG2).

^d Appears with the Metal ISM model in Pontzen & Governato (2011).

^e Appears with the H_2 ISM model in Christensen et al. (2012).

^f Appears with the H_2 ISM model in Governato et al. (2012).

^g Appears with the H_2 ISM model in Munshi et al. (2012).